Characterization and decomposition of the natural van der Waals $SnSb_2Te_4$ under compression

Juan Ángel Sans, Rosario Vilaplana, Estelina Lora Da Silva, Catalin Popescu, Vanesa Paula Cuenca-Gotor, Adrián Andrada-Chacón, Javier Sánchez-Benitez, Oscar Gomis, André Luis de Jesus Pereira, Plácida Rodríguez-Hernández, Alfonso Muñoz, Dominik Daisenberger, Braulio García-Domene, Alfredo Segura, Daniel Errandonea, Ravhi Kumar, Oliver Oeckler, Philipp Urban, Julia Contreras-García, and Francisco J. Manjón*

Dr. J. A. Sans, Dr. V. P. Cuenca-Gotor, Dr. A. L. J. Pereira, Prof. F. J. Manjón
Instituto de Diseño para la Fabricación y Producción Automatizada, MALTA-Consolider Team, Universitat Politècnica de València, Valencia, Spain

E-mail: juasant2@upv.es

Dr. R. Vilaplana, Dr. O. Gomis
Centro de Tecnologías Físicas, MALTA-Consolider Team, Universitat Politècnica de València, Valencia, Spain

Dr. C. Popescu
ALBA-CELLS, Barcelona, Spain

Dr. A. Andrada-Chacón, Dr. J. Sánchez-Benitez
Departamento de Química-Física, MALTA-Consolider Team, Universidad Complutense de Madrid, Madrid, Spain

Dr. A. L. J. Pereira
Grupo de Pesquisa de Materiais Fotonicos e Energia Renovavel - MaFER, Universidade Federal da Grande Dourados, Dourados, MS 79825-070, Brazil

Prof. P. Rodríguez-Hernández, Prof. A. Muñoz
Departamento de Física, MALTA-Consolider Team, Instituto de Materiales y Nanotecnología, Universidad de La Laguna, Tenerife, Spain

Dr. D. Daisenberger
Diamond Light Source Ltd, Oxon, England

Dr. B. García-Domene, Prof. A. Segura, Prof. D. Errandonea
Departamento de Física Aplicada-ICMUV, MALTA-Consolider Team, Universidad de Valencia, Valencia, Spain

Prof. R. Kumar
Department of Physics, University of Illinois at Chicago, Chicago IL 60607-7059, USA

Prof. O. Oeckler, Dr. P. Urban
Institut für Mineralogie, Kristallographie und Materialwissenschaft, Universität Leipzig, Germany

Dr. J. Contreras-García
CNRS, UMR 7616, Laboratoire de Chimie Théorique, F-75005, Paris, France

Keywords: metavalent bonding, high pressure, pressure-induced decomposition, electronic topological, bonding character

High pressure X-ray diffraction, Raman scattering and electrical measurements, together with theoretical calculations, which include the analysis of the topological electron density and electronic localization function, evidence the presence of an isostructural phase transition around 2 GPa, a Fermi resonance around 3.5 GPa and a pressure-induced decomposition of $SnSb_2Te_4$ into the high-pressure phases of its parent binary compounds (α-Sb_2Te_3 and SnTe) above 7 GPa. The internal polyhedral compressibility, the behavior of the Raman-active modes, the electrical behavior and the nature of its different bonds under compression have been discussed and compared with their parent binary compounds and with related ternary materials. In this context, the Raman spectrum of $SnSb_2Te_4$ exhibits vibrational modes that are associated but forbidden in rocksalt-type SnTe; thus showing a novel way to experimentally observe the forbidden vibrational modes of some compounds. Here, some of the bonds are identified with metavalent bonding, which were already observed in their parent binary compounds. The behavior of $SnSb_2Te_4$ is framed within the extended orbital radii map of BA_2Te_4 compounds, so our results pave the way to understand the pressure behavior and stability ranges of other "natural van der Waals" compounds with similar stoichiometry.

1. Introduction

The search for topological features in materials including topological insulators (TIs) and topological superconductors (TSs) is currently one of the hot topics in the Material Science field because of its interest in fundamental physics and applications in spintronics and quantum computation.[1-3] Recently, several tools have been designed to identify theoretically-predicted TI candidates and create an extensive database of compounds that exhibit these properties,[4-6] defining respective limitations and filters required by theoretical calculations to avoid false-positive predictions.[7] The discovery of 3D-TI properties in layered tetradymite-like A_2X_3

compounds, such as Bi_2Te_3, Bi_2Se_3 and Sb_2Te_3 compounds[3,8,9] and the trivial insulating behavior of Sb_2Se_3[10] have opened the question about which is the electronic and structural origin and the limiting factors of this conduct, compared to other similar materials, such as the layered tetradymite-like BA_2X_4 compounds.

Binary A_2X_3 layered compounds are usually *p*-type semiconductors with a narrow gap, leading to a high electrical conductivity.[11] In particular, α-Sb_2Te_3 and α-Bi_2Te_3 are the best thermoelectric materials near room temperature found to date,[12,13] since they feature a very small thermal conductivity. Additionally, the hybridization between the valence and the conduction band states favored by a large spin-orbit coupling (SOC) and a small bandgap, leads to the formation of Dirac cones in the electronic band structure that is responsible for their 3D-TI properties.[8] The TI properties observed in A_2X_3 binary compounds with layered tetradymite-like $R\bar{3}m$ structure [space group (s.g.) 166, Z=3] have triggered the exploration of ternary BA_2X_4 compounds based on those materials.[8, 14-16] These ternary compounds are expected to show richer physics than their binary counterparts, plus the possibility to tune their properties in a finer way by selecting appropriate *B* atoms. In fact, 3D-TI behavior has been predicted in many BA_2X_4 compounds[11,14-19] and rhombohedral $SnSb_2Te_4$ with layered tetradymite-like structure has been found to be a *p*-type 3D-TI.[11]

The tetradymite-like structure of binary A_2X_3 compounds is a 2D layered structure formed by blocks composed by five layers (*X*1–*A*–*X*2–*A*–*X*1) and called *quintuple* layer (*QL*), being *A* and *X* the cation and the anion, respectively, and *X*1 and *X*2 the two non-equivalent anions in the unit cell. These *QL*s pile up along the trigonal *c* axis and are traditionally considered to be linked by van der Waals (vdW) forces leading to the 3D material.[8]

In ternary BA_2X_4 compounds the tetradymite-like $R\bar{3}m$ structure is formed by replacing the central anion (*X2*) of A_2X_3 compounds with a three-atoms sub-block (*X2*-*B*-*X2*). In this way, the block is composed of seven layers (*X1–A–X2–B–X2–A–X1*) and called *septuple* layer *(SL)*.[20] In these ternary compounds, the tetradymite-like structure can be described by two octahedra

formed by *A* and *B* cations surrounded by six *X1/X2* and *X2* anions, respectively. In fact, these ternary compounds with tetradymite-like layered structure define a new family of materials, named "natural van der Waals heterostructures", whose nanosheets promise novel and interesting properties.[21]

Due to their technological interest, the thermoelectric properties of some layered tetradymite-like BA_2X_4 compounds have been studied[21-25] and experimental results have shown that there is a certain disorder in the crystal structure.[17, 26-31] In particular, $SnBi_2Te_4$ and $SnSb_2Te_4$ are the BA_2X_4 materials showing the smaller cation exchange in their atomic sites.[23,31,32] Noteworthy, some BA_2X_4 compounds, like rocksalt-type $SnSb_2Te_4$ and $GeSb_2Te_4$, have revealed strong properties as phase change materials since they are able to rapidly change between an amorphous and a crystalline state by light irradiation or current application. In particular, $SnSb_2Te_4$ crystallizes predominantly in the rhombohedral $R\bar{3}m$ structure (s.g. 166, Z=3) while a smaller fraction crystallizes in the metastable rocksalt-type $Fm\bar{3}m$ structure (s.g. 225, Z=4). Additionally, it can be stabilized in an amorphous phase with average octahedral coordination in the short-range order.[33] It must be stressed that both polymorphs of $SnSb_2Te_4$ (also $GeSb_2Te_4$) and its binary parent compounds, rhombohedral $R\bar{3}m$ α-Sb_2Te_3 and rocksalt-type $Fm\bar{3}m$ SnTe (c-SnTe), do not accomplish the Lewis-octet rule. Consequently, some of them have been proposed to be incipient metals by showing the recently discovered metavalent bonding;[34-37] a matter still under debate.

High pressure (HP) studies have been conducted in rocksalt-type $SnSb_2Te_4$ and $GeSb_2Te_4$[38] and in rhombohedral $SnBi_2Te_4$.[39] A pressure-induced amorphization (PIA) was reported in rocksalt-type $SnSb_2Te_4$ ($GeSb_2Te_4$) upon compression above 11 (15) GPa,[38] whereas a pressure-induced electronic topological transition (ETT) has been suggested to occur in rhombohedral $SnBi_2Te_4$.[39] Despite these efforts, many questions have yet to be addressed for the rhombohedral BA_2X_4 compounds and in particular for $SnSb_2Te_4$, including its recently

proposed superconducting character at HP.[40] For instance, "how does the presence of the new $SnTe_6$ octahedron in rhombohedral $SnSb_2Te_4$ affect the properties of the host Sb_2Te_3 structure?" and "how does rhombohedral $SnSb_2Te_4$ behave under compression?". In this scenario, we wonder if pressure on rhombohedral $SnSb_2Te_4$ leads to: i) a simple compression of the material remaining in the original structure; ii) an isostructural phase transition (IPT) followed by a structural phase transition (PT) towards a different structure, like in its parent compound Sb_2Te_3; iii) an ETT, similar to its counterpart $SnBi_2Te_4$; iii) a PIA, reported in rocksalt-type $SnSb_2Te_4$; or even iv) a pressure-induced decomposition (PID).

In this work, we report the room-temperature structural, vibrational and electrical properties of $SnSb_2Te_4$ under compression from an experimental and theoretical point of view by means of angle-dispersive X-ray diffraction (ADXRD), Raman scattering (RS) and transport measurements complemented with DFT *ab-initio* calculations and a thorough analysis of the electron density. We will show the good agreement between both experimental and theoretical descriptions and a comparison of the behavior of this material under compression has been compared to that of its parent binary compounds (α-Sb_2Te_3 and c-SnTe). We will pay special attention to the evolution of the interlayer vdW interaction under compression, considering this feature the key element to understand the behavior of the *c*/*a* ratio under compression and the stability pressure range of its low-pressure (LP) phase. Moreover, we will demonstrate that $SnSb_2Te_4$ undergoes a pressure-induced IPT near 2 GPa followed by a PID above 7 GPa. The contextualization of this result on the framework of the ternary BA_2X_4 compounds can shed light on their behavior under compression. Finally, we will show that the RS of $SnSb_2Te_4$ and its comparison with the theoretical vibrational properties of $SnSb_2Te_4$ and those of its parent compounds has revealed that: i) there is a Fermi resonance around 3.5 GPa, similar to what occurs in c-SnTe, and ii) the Raman spectrum of $SnSb_2Te_4$ shows some vibrational modes similar to those of forbidden c-SnTe. This result evidences a novel procedure to experimentally observe the forbidden vibrational modes of some materials. Finally, we will analyze the

electronic topology of the different bonds found in $SnSb_2Te_4$ together with its evolution under pressure and show that this compound behaves like the recently proposed incipient metals.

2. RESULTS AND DISCUSSION

2.1. X-ray diffraction under pressure

2.1.1. LP phase

As already commented, $SnSb_2Te_4$ usually crystallizes in rhombohedral $R\bar{3}m$ polymorph following a $GeSb_2Te_4$ structure-type with four atoms at the independent Wyckoff sites (Sn at 3a and Sb, Te1 and Te2 at 6c). A clear scheme of the polyhedral arrangement for the $GeSb_2Te_4$-type structure is shown in **Figure 1**, together with a description of the different layers composing this compound. The experimental ADXRD pattern at room conditions (see **Figure S1** in Supplemental Material (SM)) has been fitted with a von Dreele-type Le Bail refinement, which yields a trigonal unit-cell volume of 662.7(7) $Å^3$ with lattice parameters a= 4.2977(1) Å and c= 41.43(4) Å. These values are in good agreement with those reported in the literature and obtained from theoretical simulations (see **Table 1**).

Two ADXRD experiments were carried out by employing helium (up to 37 GPa) and silicone oil (up to 12 GPa) as a pressure-transmitting medium (PTM). The latter experiment up to 12 GPa (experiment 2) was performed in order to conduct a more detailed study of the LP phase. ADXRD patterns of $SnSb_2Te_4$ at different pressures from experiment 2 are shown in **Figure S1** in SM.

In **Figure S1** it is possible to observe a clear shift of the Bragg reflections of the LP phase of $SnSb_2Te_4$ towards higher 2θ angles with increasing pressure. This feature occurs due to the monotonous decrease of the distances between crystallographic planes with compression. A clear change in the diffraction patterns above 7 GPa suggests that the LP phase is no longer stable. We want to stress here that the lack of Rietveld refinement of our measurements prevents us from obtaining the experimental atomic positions in $SnSb_2Te_4$. Consequently, we have used

the atomic positions of our calculations to discuss the pressure dependence of many parameters in order to understand the behavior of $SnSb_2Te_4$ under compression. The good agreement between the experimental and theoretical pressure dependence of the unit cell volume, lattice parameters and the *c*/*a* ratio discussed in the following paragraphs, assures us of the accuracy of our theoretical data for further considerations.

The pressure dependence of the experimental and theoretical unit cell volume and lattice parameters of $SnSb_2Te_4$ of the two experiments is displayed in **Figures 2a and 2b**, respectively. The slight discrepancy observed in both figures between the values obtained using helium and silicone oil as PTM can be explained by the typical pressure uncertainty in these experiments (~ 0.5 GPa). The experimental unit cell volume (of both experiments) was fitted to a third-order Birch-Murnaghan equation of state (BM-EoS) with a B_0' higher than 4, as suggested by the positive trend of the F-f plot calculated from EoSFIT.[41] The experimental BM-EoS (see **Figure 2a**) yields a zero-pressure unit cell volume, V_0, and bulk modulus, B_0, of 663.1(6) $Å^3$ and 31.6(4) GPa, respectively. These values are in good agreement with our calculations (see **Table 1**).

The similar features of the layered structure of $SnSb_2Te_4$ and its parent binary compound α-Sb_2Te_3 suggests that the compressibility of the former must be related to that of the latter. More precisely, the compression of the former should be a combination of the compression of the $SbTe_6$ polyhedral units, also present in α-Sb_2Te_3, and of the $SnTe_6$ polyhedral units (a quasi-regular $SnTe_6$ octahedron) in the center of the *SL*, also present in c-SnTe compound. This hypothesis is supported by the similar volume compressibility of both $SnTe_6$ and $SbTe_6$ octahedral units in $SnSb_2Te_4$ and those occurring in its two parent binary compounds as shown in **Figure S2** in SM.

The evolution of the theoretical interatomic distances of $SnSb_2Te_4$ at HP (**Figure S3** in SM) shows that the Sn-Te interatomic distance inside the quasi-regular $SnTe_6$ octahedron compresses at a similar rate than the Sn-Te distances in c-SnTe ($B_0 \approx$ 50 GPa).[42] Since the Sn-

Te distance is the second less compressible interatomic distance of the $SnSb_2Te_4$ structure, it can be assumed that the compressibility of $SnSb_2Te_4$ is mostly determined by the compressibility of α-Sb_2Te_3. This hypothesis is confirmed by both experimental and theoretical data, shown in **Table 1**. Note that α-Sb_2Te_3 shows an experimental average B_0 of 36.1(9) GPa[43] that is in very good agreement with the experimental bulk modulus of $SnSb_2Te_4$. In conclusion, the compressibility of $SnSb_2Te_4$ is dominated by the α-Sb_2Te_3 component due to harder behavior of the intercalated $SnTe_6$ octahedron.

The experimental B_0 of $SnSb_2Te_4$ is similar to that of the isostructural compound $SnBi_2Te_4$ (B_0= 35(2) GPa).[39] This result implies that the compressibility of these two layered BA_2X_4 compounds is almost independent of the *A* cation and fully dependent on geometrical factors of the layered structure. A close look at the pressure dependence of the theoretical interatomic distances in **Figure S3** shows a much larger compression of the Te1-Te1 interlayer distance than that found for the Sn-Te and Sb-Te intralayer distances. Therefore, the bulk compressibility of $SnSb_2Te_4$ (also for $SnBi_2Te_4$) is dominated by the compressibility of the vdW gap between the *SL*s. The compressibility of the Te1-Te1 interlayer distances is similar for both $SnSb_2Te_4$ and α-Sb_2Te_3, in good agreement with the similar bulk compressibilities of both compounds, shown in **Table 1**. In conclusion, the compressibility of $SnSb_2Te_4$ is dominated by the strong compression of the Te-Te interlayer distance, assumed to be governed by vdW interactions, and consequently is similar to that of α-Sb_2Te_3 and $SnBi_2Te_4$.

Regarding the evolution of the experimental and theoretical lattice parameters at HP (see **Figure 2b**), they can be fitted to a modified BM-EoS in order to reproduce their sub-linear behavior. **Table 2** summarizes the axial bulk modulus, B_{0i}, and the axial compressibility as $\kappa_i = \frac{1}{3B_{0i}}$ obtained for each lattice parameter. At room conditions, $\kappa_c \sim 2\kappa_a$ is consistent with the much larger compression of the Te1-Te1 interlayer distance along the *c*-axis than the Sn-Te and Sb-Te intralayer distances in the *a*-*b* plane (**Figure S3**). Such a hypothesis is further

substantiated by the evolution of the different interplanar distances along the *c*-axis (see **Figure S4**), which allows us to identify the different contributions to the compressibility of the *c*-axis. The strong reduction of the interplanar compressed Te1-Te1 distance when compared with the behavior of the overall interplanar distances corroborates that the Te1-Te1 interplanar distance dominates the compression along the *c*-axis. Moreover, a fit of the interplanar Te1-Te1 distance with a modified BM-EoS yields a bulk modulus of 21(1) GPa that is similar to that of the *c*-axis (23.8(4) GPa). Therefore, we can conclude that the interplanar Te1-Te1 distance, assumed to be determined by the vdW interaction, is the main source for the compressibility of the unit cell along the *c*-axis and that the stronger reduction of the Te1-Te1 distance than the Sb-Te1 or Sb-Te2 distance is also the responsible for the much larger compressibility along the *c*-axis than along the *a*-axis.

Additional support to the interpretation provided in the previous paragraph is obtained by comparing the experimental and theoretical B_{0i} and κ_i of $SnSb_2Te_4$ with those of $SnBi_2Te_4$[39] and α-Sb_2Te_3[43,44] presented in **Table 2**. The close similarity of the values of the B_{0i} and κ_i in the three compounds supports the presence of similar mechanisms of compression and a similar strength of the interatomic interactions in all of them.

It is noteworthy of mentioning that the compression of the *c*-axis in $SnSb_2Te_4$ does not imply a compression of all the interplanar distances along the *c*-axis. Despite the decrease of the Sb-Te1 interatomic distance for $SnSb_2Te_4$ (see **Figure S3**), the interplanar Sb-Te1 distance expands under compression and the same occurs for α-Sb_2Te_3 (see **Figure S4**). This feature clearly suggests an increase of the angle between the *ab*-plane and the Sb-Te1 bond at HP that distorts the $SbTe_6$ octahedron as clearly observed in **Figure S5a** in SM. We also intend to highlight that although the Sb-Te1 interatomic distance shows the same pressure dependence in $SnSb_2Te_4$ and α-Sb_2Te_3, the presence of the short Sn-Te bond in $SnSb_2Te_4$ triggers a slight increase of the Sb-Te2 interatomic distance, and a consequent larger decrease of the Sn-Te bond with pressure

than in c-SnTe. This result means that there is a slightly larger and weaker Sb-Te2 bond in $SnSb_2Te_4$ than in α-Sb_2Te_3. This variation caused by the chemical pressure induced by the combination of the binary parent compounds (c-SnTe and α-Sb_2Te_3) in the formation of $SnSb_2Te_4$, can also be understood through the change in the orientation of the lone electron pair (LEP) of Sb, which can induce a slight distortion of the $SbTe_6$ polyhedral unit. This distortion is small because the compressibility of the Sb-Te2 interatomic distance for both $SnSb_2Te_4$ and α-Sb_2Te_3 compounds follows a similar pattern.

A good agreement between experimental and theoretical data is also found for the evolution of the *c*/*a* ratio at HP (see the inset of **Figure 2b)**. This ratio shows a clear change of tendency above 2 GPa similar to that observed in α-Sb_2Te_3[43,44] and $SnBi_2Te_4$.[39] The minimum of the *c*/*a* ratio in $SnSb_2Te_4$ can also be explained by analyzing the pressure dependence of respective interplanar distances along the *c*-axis (see **Figure S4**). In particular, the evolution of the Te1-Te1 interplanar distance in $SnSb_2Te_4$ shows a strong (normal) compression below (above) 2 GPa. This behavior is typically associated with the weak character of the vdW bonds at LP and its hardening due to the increase of the covalent character of the Te-Te bonds at HP.[45] A similar conduct of the *c*/*a* ratio is observed for α-Sb_2Te_3 since the Sb-Te interplanar distances evolve in this compound in a similar manner as in $SnSb_2Te_4$ (see **Figure S4**). Therefore, we can conclude that the change of the compression rate of the interlayer space (caused by the change of the compressibility of the Te1-Te1 interplanar distance) gives rise to the *c*/*a* ratio minimum observed in $SnSb_2Te_4$ and α-Sb_2Te_3. The evolution of the vdW character of the interlayer bonds at HP will be addressed in depth later on, when we discuss the analysis regarding the dependence of the electronic topology at HP.

The big change in the slope of the *c*/*a* ratio in $SnSb_2Te_4$ and related compounds at HP is likely related to a pressure-induced IPT. We must recall that these chalcogenides are mainly composed by group-15 cations acting with their lowest valence state and featuring a strong cationic LEP

stereoactivity that has a deep effect in the formation of the 2D layered structure. The presence of the cationic LEP modifies the electronic distribution of the charges in the crystal and distorts the geometry of the bonds. Moreover, the cationic LEP is mainly oriented along the *c*-axis in these compounds and contributes to the vdW interaction between the layers and to the strong compressibility of the *c*-axis at LP since the LEP is extremely compressible at LP. This scenario has been already observed in a number of group-15 sesquichalcogenides.[46,47] Additionally, it has been widely reported that both the cationic LEP and the vdW interaction become more incompressible at HP due to the progressive decrease of the LEP activity and the increase of the strength of the interlayer forces. Therefore, it can be considered that these changes in compressibility of electronic 'density-clouds' at relatively LP lead to a new isostructural phase with a different *c/a* ratio in $SnSb_2Te_4$ and related chalcogenides, and these can be understood as an IPT of electronic origin, as we will further show.

A different way of understanding the structural behavior of $SnSb_2Te_4$ at HP is by studying the compression of the two octahedral units forming the $SnSb_2Te_4$ heterostructure: the regular octahedron around Sn and the slightly deformed octahedron around Sb (see **Figure 1**). **Figure S6** in SM shows the evolution of the theoretical quadratic elongation of both octahedra at HP. This parameter was defined by Robinson *et al*[48] to analyze the distance of the inner atom of a polyhedron with respect to the central position, which is an indirect measurement of the irregularity of the polyhedral unit. In our case, the $SnTe_6$ ($SbTe_6$) octahedron shows practically no changes in the quadratic elongation up to 2 GPa and an increase above 2 (4) GPa. This result suggests that both octahedra are almost insensitive to pressure while there is a strong compression of the vdW interlayer gap below 2 GPa. Nevertheless, $SnTe_6$ octahedra show a considerable increase of the polyhedral distortion above 2 GPa; once the vdW gap becomes as incompressible as the octahedral units. Therefore, results of **Figures S5** and **S6** support the occurrence of a pressure-induced IPT near 2 GPa in $SnSb_2Te_4$.

Finally, in order to measure the differences of the interatomic distances in both octahedra with respect to those in a regular coordination, we have plotted in **Figure S7** the evolution of the theoretical distortion index of both octahedra at HP.[49] It can be observed that the regular $SnTe_6$ octahedron remains regular during the whole compression process while the distorted $SbTe_6$ octahedron becomes slightly more regular under compression. This is a consequence of the evolution of the Sb-Te1 and Sb-Te2 distances under compression, which tend to follow a similar pattern, but at a smaller rate. In summary, we have shown that the own definition of the $SnSb_2Te_4$ heterostructure as a layered distribution of *SL*s makes it essential to analyze the polyhedral units and the inter- and intra-layer compressibility in order to understand respective behavior at HP.

To close this section, we have plotted the experimental quadratic elongations of the AX_6 and BX_6 octahedra of all BA_2X_4 compounds known to have the $R\bar{3}m$ structure at room pressure according to the ICSD database (see **Figure 3**). In this way, we can try to shed light on the HP behavior of the compounds of this ternary family. It can be observed that $SnSb_2Te_4$ is one of the compounds with the smallest quadratic elongation of the AX_6 octahedron ($SbTe_6$) and conversely with the largest quadratic elongation of the BX_6 octahedron ($SnTe_6$). Therefore, according to the trend observed in the theoretical quadratic elongation of both octahedra at HP (see **Figure S6**), it can be deduced that $SnSb_2Te_4$ will behave at HP similar to $PbSb_2Te_4$ at LP, while $SnBi_2Te_4$ tends to behave at HP as $GeSb_2Te_4$ at LP.

Regarding the **Figure 3**, more conclusions can be drawn. *A priori*, it could be thought that the AX_6 quadratic elongation should decrease in the sequence As-Sb-Bi due to the larger stereoactivity of the LEP in As than in Sb and Bi. This fact is due to the stronger hybridization of the cationic s-p levels in As than in Sb and Bi for a given atom.[50] On the other hand, it could be also thought that the BX_6 quadratic elongation should decrease in the sequence Pb-Sn-Ge due to the larger difference between the s-p levels in Pb than in Sn and Ge.[50] Unexpectedly, the above arguments seem not to be true since $SnBi_2Te_4$ (with a common *B* cation with

$SnSb_2Te_4$) has a larger AX_6 quadratic elongation, whereas $GeSb_2Te_4$ (with a common A cation with $SnSb_2Te_4$) has a smaller BX_6 quadratic elongation and a much larger AX_6 quadratic elongation. Therefore, results of **Figure 3** suggest that there is a close relationship between the quadratic elongation of the AX_6 and BX_6 octahedra in these compounds and that not all combinations of AX_6 and BX_6 quadratic elongations compatible with the $R\bar{3}m$ structure. This hypothesis is supported by the lack of compounds $PbAs_2Te_4$ and $SnAs_2Te_4$ with $R\bar{3}m$ structure, which should be located in the upper right region in the diagram; i.e. far away from the red line marking the average of the possible AX_6 and BX_6 quadratic elongations. A similar reasoning can be applied to explain why $PbSb_2Se_4$, $SnSb_2Se_4$, $PbBi_2S_4$ and $SnSb_2S_4$ cannot crystallize in the $R\bar{3}m$ structure.[51-53] In this context, it must be recalled that the LEP activity of group 15 cations increases when the anion follows the sequence Te-Se-S-O.[50] Therefore, taking into account the energetic difference between the p-levels of the anion and the s-levels of the cation, the strong LEP stereoactivity of As in tellurides should be similar to that of Sb cation in selenides and sulfides and to that of Bi in sulphides and oxides, taking into account the energetic difference between the p-levels of the anion and the s-levels of the cation. Consequently, this strong cation LEP stereoactivity allows us to explain why the above-mentioned compounds do not crystallize in the $R\bar{3}m$ phase.

2.1.2. Pressure-induced decomposition (PID)

Above 7 GPa, a clear change of the experimental XRD patterns occurs. The disappearance of Bragg reflections around 11 and 14.6 degrees and the appearance of new peaks at 8.6 and 10.1 degrees (at 10.8 GPa) without showing a relevant peak broadening suggests the absence of a PIA. Thus, the only two possibilities are a PT or a PID.

In order to probe possible crystalline HP phases after a PT, we have resorted to the structure field map of BA_2Te_4 compounds reported by Zhang *et al.*,[54] with ternary compounds systematically ordered according to the cationic orbital radii, R_B and R_A.[55] This structure field

map (see **Figure 4**) allows us to understand and predict the structures of ternary BA_2Te_4 compounds at LP by knowing R_B and R_A. Moreover, it can help in predicting the HP phases if we know how orbital radii behave at HP. In the field map of Zhang *et al.*, materials with $R_B \in$ [1.6, 1.9] a.u. and $R_A \in$ [1.0, 2.0] a.u. crystallize in the b37 structure (s.g. $R\bar{3}m$); however, new tellurium-based ternary chalcogenides formed by different group-14 *B* cations (*B* = Ge, Sn and Pb) group-15 *A* cations (*A* = As, Sb and Bi) also crystallize in s.g. $R\bar{3}m$ according to the ICSD database. This are the cases of $GeAs_2Te_4$ (with R_B=1.415 a.u. and R_A=1.560 a.u.) and $PbBi_2Te_4$ (with R_B=1.997 a.u. and R_A=2.090 a.u.). We have included these two compounds in the structure field map because they limit the new borders of materials with s.g. $R\bar{3}m$. In this way, we can extend the stability ranges of the b37 structure to $R_B \in$ [1.4, 2.0] a.u. and $R_A \in$ [1.0, 2.1] a.u. with respect to the structure field map reported by Zhang *et al.*[55]

The new structure field map of BA_2Te_4 compounds allows us to consider several possible HP phases for a compound with an initial $R\bar{3}m$ structure. The most important ones are the spinel b4 structure (s.g. $P\bar{4}2m$ or $I\bar{4}$) and the monoclinic d3 structure (s.g. *C2/m*). It is noteworthy to highlight that one of the parent binary compounds of $SnSb_2Te_4$ (α-Sb_2Te_3) has the $R\bar{3}m$ structure and undergoes a PT towards a *C2/m* structure (β-Sb_2Te_3).[56] Therefore, the latter phase could be a good candidate for the ternary compound $SnSb_2Te_4$ to crystallize in. The same reasoning applies to $SnBi_2Te_4$ since α-Bi_2Te_3 also has the $R\bar{3}m$ structure and undergoes a PT towards a *C2/m* structure (β-Bi_2Te_3).[56] Nevertheless, all our attempts to identify the possible HP phase through theoretical simulations failed.

Subsequently, we have considered the possibility of a PID. For this purpose, we have calculated the formation enthalpy of $SnSb_2Te_4$ in s.g. $R\bar{3}m$ and compared it with those of the HP phases of its binary compounds (**Figure 5**). We have found that above 6.3 GPa the combination of the HP phases β-SnTe (s.g. *Pnma*) and β-Sb_2Te_3 (s.g. *C2/m*) is energetically more favorable than the LP phase of $SnSb_2Te_4$. This result suggests that the ternary compound $SnSb_2Te_4$ should

decompose into their parent binary materials above 6.3 GPa. In fact, we have found that the ADXRD patterns observed above 7 GPa in $SnSb_2Te_4$ (**Figure S1**) exhibit a perfect fit with the HP phases of the binary parent compounds. A similar theoretical result has been obtained for $SnBi_2Te_4$ (see **Figure 5**), thus suggesting that also PID should be observed in $SnBi_2Te_4$ above 7 GPa.

It must be stressed that PID is not a common phenomenon occurring at room temperature, unlike PIA. In fact, similar compounds like $Ge_2Sb_2Te_5$ undergo PIA at room temperature.[57] The PIA at room temperature is mainly due to the frustration of either a PT to a HP phase or a PID into daughter compounds.[58] This frustration mainly occurs due to kinetic features governed by temperature. In fact, PID is usually observed in complex compounds mostly at high temperature[59-62] or in some molecular materials, such as H_2S, where PID occurs at room temperature and at very HP.[63] $SnSb_2Te_4$ is one of the few compounds exhibiting PID at room temperature and relatively LP (7 GPa). This result might be related to the large stability of their polyhedral units that prevail after the PID.

We want to finish by pointing out that the PID of rhombohedral $SnSb_2Te_4$ into their binary compounds may explain the superconducting properties recently proposed for this material above 8 GPa,[40] since β-Sb_2Te_3 exhibits a similar superconducting character around the same pressure.[64] Thus, β-Sb_2Te_3 may be responsible for the superconducting properties associated to $SnSb_2Te_4$.[65]

2.2. Raman scattering measurements under pressure

In order to corroborate the results found in the structural study under pressure, we performed unpolarized HP-RS measurements. Since there is one formula unit (7 atoms) in the primitive unit cell of $SnSb_2Te_4$, this compound has twenty-one normal vibrational modes at Γ with the following mechanical decomposition:[66]

$$\Gamma = 3\ A_{1g}(R) + 3\ A_{2u}(IR) + 3\ E_u(IR) + 3\ E_g(R) + A_{2u} + E_u$$

where E modes are doubly degenerated, A_{1g} and E_g modes are Raman-active (R) and A_{2u} and E_u are IR-active except for one A_{2u} and one E_u mode that correspond to the three acoustic phonons considering that E-type modes are doubly degenerated. Therefore, there are six Raman-active modes (Γ_{Raman}= $3A_{1g}$ + $3E_g$) and six IR-active modes (Γ_{IR}= 3 A_{2u} + 3 E_u). The assignment of the vibrational modes to atomic movements was done through the interface of Jmol Interface for Crystallographic and Electronic Properties (J-ICE)[67] and is discussed in the SM (see **Figures S8** to **S17**).

Figure S18 shows the unpolarized RS spectrum of $SnSb_2Te_4$ at room conditions together with the position of the theoretically predicted frequencies at these conditions (see vertical bottom tick marks). The RS spectrum at room conditions shows five of the six theoretically predicted Raman-active modes. A rather good agreement between the experimental and theoretical Raman-active mode frequencies at room pressure are observed (see also **Table S1**). Consequently, we have made a tentative assignment of experimental Raman modes considering the predicted frequencies and pressure coefficients as discussed below.

it is well known that in layered materials vibrational modes at the Γ point can be classified into interlayer modes (in the low-frequency region) and intralayer modes (in medium- and high-frequency regions). Moreover, layered compounds crystallizing either in rhombohedral, hexagonal or tetragonal space groups, show A (or B) and E modes. In rhombohedral $SnSb_2Te_4$, there are two pure interlayer modes (E_g^1 and A_{1g}^1), which have the lowest frequencies, and the other ten Raman- and IR-active modes are intralayer modes and have both medium and high frequency values (see **Table S1** and **Table S2**). The two interlayer modes, also known as rigid layer modes, correspond to out-of-phase movements of the neighbor layers both along the *a*-*b* plane (E_g^1 mode) and along *c*-axis (A_{1g}^1 mode).

Figure S18 also shows the unpolarized HP-RS measurements up to 9 GPa. Pressure induces a monotonous shift of the Raman modes towards higher frequencies, except for two modes with negative slope near ambient pressure (see **Figure 6**). These two modes can be unambiguously

assigned to metallic Te[68] and their appearance can be explained by the extreme sensitivity of some selenides and tellurides to visible laser radiation. In fact, Raman modes of trigonal Se and Te with negative slope have been recently identified in HP-RS studies of As_2Te_3[47] and $HgGa_2Se_4$.[69]

The pressure dependence of the experimental and theoretical Raman-active modes in $SnSb_2Te_4$ at HP (see **Figure 6** and **Table S1**) shows a good agreement within a 5% accuracy interval. This feature is a clear sign of the good description reached by the *ab-initio* simulations for this compound. For the sake of completeness, the evolution of the theoretical IR-active modes in $SnSb_2Te_4$ is also given in **Figure S19** and **S20** in SM.

Similar vibrational modes in the low- and high-frequency ranges of $SnSb_2Te_4$ are also observed in the parent binary compound α-Sb_2Te_3 (see **Figure S21** and **Tables S1** and **S2**). However, there are four vibrational modes of $SnSb_2Te_4$ in the medium-frequency region (two Raman-active and two IR-active) that do not have correspondence on the α-Sb_2Te_3 compound, because they are characteristic of the *SL* in ternary layered BA_2X_4 compounds. These extra modes in $SnSb_2Te_4$ arise from the vibrations involving the central Sn-Te2 bonds; in particular, out-of-phase vibrations of the Te2 atoms of the $SnTe_6$ polyhedral unit (see **Figures S10 and S11**).

It is well-known that the rocksalt-type structure of c-SnTe does not have any Raman-active mode but one IR-active mode with T_{1u} symmetry that splits into a doubly degenerate transverse optical (TO) mode and a single longitudinal optical (LO) mode. It is interesting to note that the two extra modes observed in $SnSb_2Te_4$ can be related to the two IR-active modes of c-SnTe (see **Figure S22**). In this context, it can be observed that phonons of similar nature in $SnSb_2Te_4$ and α-Sb_2Te_3 are located around similar frequencies (**Figure S21**), so the position of the two medium-frequency modes in $SnSb_2Te_4$ is expected to be located at similar frequencies than in c-SnTe. In particular, there is a clear correlation between the A_{1g}^2 mode of $SnSb_2Te_4$ and the LO-type IR-active mode of c-SnTe at room pressure[70] (see **Table S2**) that is also extended at

HP (see **Figure S22**). Therefore, our Raman results for $SnSb_2Te_4$ open a new way to characterize the lattice dynamics of binary compounds with forbidden Raman modes, like those crystallizing in the rocksalt-type structure as c-SnTe, by means of RS measurements in more complex compounds containing similar atomic coordination as those in the binary compounds. A similar example may be the case of rocksalt-type MgO, whose LO IR-active mode (738 cm^{-1})[71] is consistent with the frequency of the highest Raman-active mode (715 cm^{-1}) in $MgTiO_3$ with s.g. $R\bar{3}$.[72]

An anomalous decrease of the experimental and theoretical frequency of Raman-active modes A_{1g}^2 and E_g^2 (see **Figure 6**) and of the theoretical frequency of IR-active modes E_u^2 and A_u^2 (see **Figure S19**) of $SnSb_2Te_4$ is observed above 3.0 GPa. The softening of these vibrational modes, mainly related to Sn-Te vibrations could be *a priori* ascribed to the pressure-induced IPT around 2 GPa, which is similar to that occurring in α-Sb_2Te_3 between 2.5 and 3.5 GPa.[43,73,74] A close look at our theoretical simulations (see **Figures S10 and S11**) reveal that the E_g^2 and E_u^2 modes in $SnSb_2Te_4$ are mainly Sn-Te bending modes with a slight stretching contribution, while the A_{1g}^2 and A_{2u}^2 modes are mainly Sn-Te stretching modes. Since stretching modes mainly depend on the bonding force constant and the bonding distance, the softening of these vibrational modes involving Sn-Te2 bonds could likely be related either to a strong decrease of the Sn-Te2 bonding force constant (depending on the charge density) or to a strong increase of the interatomic distance. However, neither an increase of the Sn-Te2 interatomic distance (**Figure S3**) nor a decrease of the Sn-Te2 bond charge density (**Figure S26**) have been observed in the whole studied pressure range. Another possibility to explain the softening is that there is a change of the character of the stretching modes so that they become more bending-like than stretching-like. To prove that, we have looked at the angle between the *ab*-plane and the Sn-Te2 bond (see **Figure S5b**). It can be observed that a subtle change in this angle occurs around 4 GPa but the increase of the angle value suggests that these vibrational

modes acquire an increasing stretching character, which is incoherent with the loss of bonding strength.

After all these considerations, we have concluded that the softening of the medium-frequency phonons in $SnSb_2Te_4$ could only be explained by a Fermi resonance effect.[75] A Fermi resonance occurs when there is a strong anharmonic interaction of a first-order phonon with a two-phonon combination containing a high density of states. In such a case, a frequency shift and a change in the intensity and width of the first-order vibrational mode occurs. The Fermi resonance is a rare phenomenon in solids that has been observed in copper halides, molecules and defect modes.[76-79] In $SnSb_2Te_4$, the sum of the frequencies of the A_g^1 and E_g^1 at Γ almost coincides in frequency with the E_g^2 mode at 2 GPa; i.e. the pressure range close to the onset of the softening of this mode in $SnSb_2Te_4$ (**Figure 6**). The anomalous softening of the Sn-Te related modes in $SnSb_2Te_4$ is also reproduced, even more clearly, by the theoretically predicted evolution of the IR-active LO-mode of c-SnTe at HP (see **Figure S22**). Note that the frequency of this mode in c-SnTe coincides in frequency at Γ with twice the value of the TO mode when a sudden change of trend occurs (**Figure S22**). Therefore, we conclude that c-SnTe exhibits a Fermi resonance in the IR-active LO mode that is also reproduced in the medium-frequency range of $SnSb_2Te_4$. This result gives further support to our previous interpretation of the relationship between the vibrational modes of $SnSb_2Te_4$ and c-SnTe. In summary, we attribute the softening of A_g^2 and E_g^2 of $SnSb_2Te_4$ at HP to a pressure-induced Fermi resonance caused by the coincidence of the frequencies of these firs-order Raman modes and the combination of A_g^1 and E_g^1 modes along the whole BZ.

To close this section, we have calculated the phonon dispersion curves in $SnSb_2Te_4$ at 0, 2 and 4 GPa (see **Figure S23**) in order to understand the nature of the IPT close to 2 GPa previously discussed. As observed, our calculations do not show softening of any of the phonon branches. This result suggests that the pressure-induced IPT found above 2 GPa, cannot be assigned to a 2^{nd}-order IPT and must be of higher-order.

In summary, our analysis of the lattice dynamics of $SnSb_2Te_4$ at HP shows the layered character of this compound and a good agreement between our experimental and theoretical data. The Raman-active modes of $SnSb_2Te_4$ have been explained in relation to its binary parents α-Sb_2Te_3 and c-SnTe and it has been proved that modes that cannot be observed by Raman scattering in c-SnTe can be observed with this technique in $SnSb_2Te_4$ containing similar $SnTe_6$ polyhedra than c-SnTe. Additionally, the anomalous behavior of two Raman-active and two IR-active modes above 3.5 GPa in the medium-frequency region, which are characteristic of the *SLs* and related to Sn-Te vibrations, has been attributed to a Fermi resonance that also occurs in c-SnTe near 2 GPa. Finally, we have proved, with the help of the phonon dispersion curves for $SnSb_2Te_4$ at different pressures, that the IPT occurring in $SnSb_2Te_4$ close to 2 GPa is not of 2nd-order but of higher order, as expected for an IPT of electronic origin.

2.3. Electrical resistance measurements under pressure

In the parent binary compound α-Sb_2Te_3, the reported pressure-induced IPT was argued to be associated to a pressure-induced ETT around 3.5 GPa.[43] This result has motivated us to carry out resistance measurements and theoretical calculations of the electronic band structure at different pressures in order to verify if a pressure-induced ETT could be also observed in $SnSb_2Te_4$. This kind of measurements have been previously validated by other works[80] up to 50 GPa.

Two abrupt variations in the pressure dependence of the electrical resistance of $SnSb_2Te_4$ above 2 and 8 GPa have been observed (see **Figure 7**). The variation above 8 GPa can be ascribed to the PID of the sample, already commented in section A, which is similar to that observed also above 8 GPa in $SnBi_2Te_4$.[39] This result confirms our formation enthalpy analysis (**Figure 5**) that suggest that $SnBi_2Te_4$ likely undergoes also a PID. Furthermore, the low resistance measured above 8 GPa can be ascribed to the metallic nature of the HP phases of α-Sb_2Te_3 and c-SnTe.[42,81]

Below 8 GPa, we can distinguish two different ranges in the evolution of the electrical resistance of $SnSb_2Te_4$ below and above 2 GPa. At the LPs, $SnSb_2Te_4$ evidences a very low electrical resistance (constant from room pressure to 2 GPa), whose behavior and values are typical of a degenerate semiconductor. Previous results on the literature[32] have shown that these results correspond to a lack of stoichiometric vacancies, which leads to the formation of a p-type degenerate semiconductor whose carriers are created by cation vacancies. Above 2 GPa, there is a drastic increase of the electrical resistance, which traditionally has been associated in the literature to the creation of structural defects along an ongoing phase transition.[82] These defects might create a donor levels that modify the carrier concentration of the material. In $SnSb_2Te_4$, the IPT occurring around 2 GPa might be the responsible for the creation of donor levels associated to defects. These could be able to trap p-carriers, thus helping to pass from a degenerate to a non-degenerate semiconductor or acting as scattering centers that decrease carrier mobility. In any case, the decrease in carrier mobility would be an indication of a decrease of the p-type character of the electrical conduction in $SnSb_2Te_4$, similar to that occurs in ZnTe between 7-11 GPa.[82] Thus, the decrease of the conductivity evidenced by $SnSb_2Te_4$ above 2 GPa could be exploited to overcome one of the main problems of TIs; i.e. the non-observation of surface carrier conductivity, which would be masked by bulk carrier conductivity.[83]

Regarding electronic band structure calculations, we obtain that $SnSb_2Te_4$ is an indirect bandgap semiconductor with a bandgap energy E_g= 0.12 eV at room pressure, similar to that previously obtained,[16] and that the bandgap energy decreases with increasing pressure leading to a closening of the bandgap above 4.5 GPa (see **Figure S24**). Since our calculations based on Density-Functional Theory (DFT) are known to yield underestimated bandgaps when (semi-)local functionals are employed, the value of the real bandgap is expected to be above 0.2 eV at room pressure[11] and the real metallization must occur at higher pressures. In fact, the predicted lack of metallization at LP and the negative slope of the bandgap are compatible with

the above-mentioned explanation of the evolution of the electrical resistance at HP. However, we cannot neglect the fact that the lack of hydrostatic conditions above 2.5 GPa due to the use of a solid PTM may blur the interpretations of the changes observed in the electrical properties of the material.

Regarding the possibility of an ETT in $SnSb_2Te_4$, our electronic band structure calculations show that the valence band shows no major changes in the whole range of studied pressures; however, there are considerable changes in the conduction band. At 0 GPa, the conduction band minimum is around the Γ point, but there is a considerable downward shift of the local minimum of the conduction band at the F point with pressure. This minimum becomes the absolute minimum of the conduction band above 4.5 GPa. Therefore, a possible ETT could be expected for n-type material between 0 and 4.5 GPa. Since we work with a p-type material, we cannot attribute the change in resistance near 2 GPa to an ETT.

In summary, our electrical measurements in $SnSb_2Te_4$ show a small resistance at LP, typical of a degenerate semiconductor, and an increase of the electrical resistance above 2.0 GPa, attributed to the generation of defects due to the pressure-induced IPT. Finally, the decrease of the electrical resistance above 8 GPa is attributed to the metallic nature of the HP phases of α-Sb_2Te_3 and c-SnTe due to the decomposition of $SnSb_2Te_4$ above 7 GPa. The behavior of the electrical resistance in $SnSb_2Te_4$ is consistent with our calculations of the electronic band structure that do not show metallization up to 8 GPa when the value of the theoretical bandgap is corrected.

2.4. Electronic topology under pressure

Rhombohedral $SnSb_2Te_4$ contains different kind of bonds. The vdW interaction between Te1 atoms belonging to different blocks is widely accepted in the scientific community; however, recent studies in chalcogenides have established the difference in the interatomic distance with

respect to their vdW radii as an indication that this Te1-Te1 bond is not purely vdW. Thus, the assignation to this separation as vdW gap would be reinterpreted as vdW-like gap.[37,84]

The nature of the bonds between Sn-Te2, Sb-Te2 and Sb-Te1 are also the focus of intense debates. According to the Lewis' octet rule, the Sb^{3+} and Sn^{2+} cations bonds to Te^{2-} should not have the octahedral coordination observed here, and this has been explained in the literature by delocalization of the charge by means of a chalcogen or hypervalent interaction.[85,86] In our case, the bonds are not established among chalcogen atoms, but between a chalcogen anion and different kind of cations. This scenario may imply that we can neglect the chalcogen bonding as responsible for the interactions above-mentioned. On the other hand, the concept of hypervalency has been extensively studied and is a subject of strong discussions up to date. The most recent and accepted quantitative approximation to this concept was performed by Durrant,[87] where the valence equivalent electron parameter defined by "the formal shared electron count at a given atom, obtained by any combination of valid and covalent resonant form". This parameter discerns between molecules that can be considered as hypervalent or obeying a "modified octet rule". For instance, XeF_2 molecule[88] should obey a modified octet rule, the same as occurs for our SbTe6 and SnTe6 polyhedral units. The bond character for the XeF_2 molecule has been explained by the concept of a charge-shift bond, which is usually established between a central atom with low ionization potential and a strongly electronegative ligand. In our case, the SbTe6 or SnTe6 polyhedral units are described without significant difference between their electronegativities. The unfortunate attempt to describe the chemical interactions involved on these polyhedral units led us to explore new kind of bonds. Thus, the interactions in both parent binary compounds of $SnSb_2Te_4$ (α-Sb_2Te_3 and c-SnTe) have been recently explained by the so-called metavalent bonding,[34-37] where electrons are shared between nearest neighbors without electron transfer allowing to exceed the octet rule limitation. The use of this denomination is still under controversy, because some authors claimed that the bonding in chalcogenides can be explained by molecular-orbital approach or valence-bond

theory of hyperbonding,[89] where that hypervalence bonding is a special case of charge-shift bonding.[90]

2.4.1. Bader charge analysis

In recent HP works of α-Sb_2Te_3, the occurrence of a pressure-induced IPT was studied on the light of the electron density evolution under pressure.[74] Additionally, the pressure-induced ETT was interpreted on the light of the evolution of the Bader charges at HP.[73] Since the occurrence of a pressure-induced ETT depends on the location of the Fermi level, it is rather doubtful that the pressure at which an ETT is observed can be determined with the study of the theoretical Bader charge analysis, which is independent of the location of the Fermi level. However, a change in the evolution of the Bader charges at HP can be indicative of a pressure-induced IPT, not related with a variation of the Fermi level.

Figure 8a shows the pressure dependence of the Bader charges for each of the constituent atoms of $SnSb_2Te_4$. The Bader charges of the internal atoms of the *SLs* (Sn and Te2 atoms), related to the $SnTe_6$ polyhedral units, are larger than those of the external atoms of the SL (Sb and Te1) related to the $SbTe_6$ polyhedral units, and describe a monotonous trend with respect to pressure following an almost linear behavior with a small kink near 2 GPa. On the other hand, the pressure evolution of the Bader charges of the most external atoms of the *SLs* cannot be fitted to a single linear trend and two linear fits below and above 2 GPa are required.

The comparison between the polyhedral net charges contained in the two octahedral units that compose this ternary material (**Figure 8b**) reveals a clear change of trend above 2 GPa (**Figure 8c**). An abrupt charge transfer from $SbTe_6$ towards $SnTe_6$ occurs up to 2 GPa and ceases above this pressure. This evolution can be explained as follows: At LP, the closening of the inter-layer gap leads to a strong charge redistribution of the external $SbTe_6$ unit that lead to a charge transfer to the $SnTe_6$ unit. Above 2 GPa, the vdW-like space is already closed and no further charge is transferred between both $SnTe_6$ and $SbTe_6$ units so their Bader charges evolve similarly under pressure. In summary, the charge redistribution between the polyhedral units is

consistent with Te1 atoms being involved in the $SbTe_6$ octahedral units and being the ones responsible for the vdW interactions in the inter-layer gap that define the IPT around 2 GPa in $SnSb_2Te_4$.

2.4.2. Non-Covalent Interaction analysis

We have performed Non-Covalent Interaction (NCI) simulations[91,92] to probe the evolution of the low electron density regions at the inter-layer space between two neighbouring *SLs*. **Figure S25** in SM highlight the vdW-like interactions at the inter-layer (Te1-Te1) space at LP and their evolution towards more localized interactions at HP. A 2D data profile of the NCI of the inter-layer space between two *SLs* is represented in **Figure 9**. This figure can be interpreted as follows: At LP, the electron density cloud is very flat and delocalized but the fact that the interatomic distance is smaller than the vdW diameter might imply a certain localized character, even if the vdW bond is predominant. Above 2 GPa, bonds become more localized; thus, clear bonds appear among polyhedra of neighbor *SL*s. Overall, all results point at charge localization with increasing pressure so that the Te1-Te1 vdW nature of the inter-layer space is no longer governing the response of the solid above 2 GPa.

2.4.3. Electronic density analysis

A more quantitative analysis of the electronic topology can be done by analyzing the evolution of two parameters, such as the electron charge density, $\rho(\vec{r})$, and its Laplacian, $\nabla^2\rho(\vec{r})$, at the bond critical point (BCP), which can be defined by the point of minimum electron density between two bonded atoms (following the electron density gradient). This method allows us to determine the bonding character of the four bounds found in $SnSb_2Te_4$ (Te1-Te1, Sb-Te1, Sb-Te2 and Sn-Te2).

With regards to the Te1-Te1 interaction, we can distinguish its predominant vdW character at LPs, determined by a low $\rho(\vec{r})$ and a positive value of the $\nabla^2\rho(\vec{r})$ at the BCP (see **Figure S26**). However, these values are higher than those found in vdW complexes.[93] Then, we cannot

neglect that the interlayer interaction may be influenced by a certain charge transfer caused by the Sb-Te1 bond, as suggested by Cheng et al.[37] An increase of both parameters at HP is coherent with the decrease of vdW character[94] we have already observed and commented in the previous section. At LP, Te1 atoms are bonded to three Sb atoms and at close vicinity with other three Te1 atoms, belonging to the neighboring layer, at much larger distance. At HP, the strong decrease of the interlayer Te1-Te1 distance gives rise to a stronger interaction between the Te atoms belonging to different layers, thus leading to a sixfold coordination of the Te1 atoms. This Te1-Te1 interaction supports the evidence of the formation of more ionic bonds between the neighboring Te atoms since ionic bonds are characterized by large and positive $\rho(\vec{r})$ and positive $\nabla^2\rho(\vec{r})$ at the BCP (see **Table S3**).

With respect to the Sb-Te2 and Sn-Te2 bonds, they possess similar values of $\rho(\vec{r})$ and $\nabla^2\rho(\vec{r})$ at the BCP in the whole pressure range studied. In fact, the value of $\rho(\vec{r})$ for both bonds is intermediate between that of Sb-Te1 bond and the weak vdW interaction between Te1 atoms along the whole of the studied pressure range. In this context, we have to recall that both parent binary compounds, α-Sb_2Te_3 and c-SnTe, have been considered as incipient metals,[34-37] therefore these values of $\rho(\vec{r})$ and $\nabla^2\rho(\vec{r})$ could be characteristic parameters of metavalent bonding with partially delocalized electrons.

Regarding the Sb-Te1 bond, it evidences a very high $\rho(\vec{r})$ when compared to the overall interactions and a positive, although close to zero, value of the $\nabla^2\rho(\vec{r})$ at the BCP in the whole pressure range studied. The high $\rho(\vec{r})$ value is typical of covalent or ionic bondings; however, the $\nabla^2\rho(\vec{r})$ value must be negative (positive) for a covalent (ionic) bonding. Therefore, the small positive $\nabla^2\rho(\vec{r})$ value suggests a mixture between the covalent and metavalent bonding. Note that a polar covalent interaction is neglected because typically it should show a value of $\nabla^2\rho(\vec{r})$ closer to zero.

In order to deepen into the analysis of the character of these two bonds, we have plotted the ELF along the different atomic interaction distances of $SnSb_2Te_4$; namely, Te1-Te1, Sb-Te1, Sb-Te2 and Sn-Te2 (see **Figure 10** and **Figure S27**). ELF describes the character of bond formation between the involved atoms. At LPs, the low ELF values (close to 0.2) close to the center of the Te1-Te1 distance, exhibit the typical values of vdW bonds; however, this ELF signal increases rapidly with pressure towards values characteristic of an ionic-type bond in good agreement with the results observed from the BCP electronic topological analysis. In the case of the Sb-Te1 bond, the ELF value close to the center of its respective interatomic distance is high enough (0.7) to ensure we are dealing with a strong bond, coherent with the polar-covalent results previously obtained from the BCP analysis.

Regarding the ELF signals between the Sn-Te and the Sb-Te2 bonds, these have a medium value (0.5-0.6), which is close to the center of the interatomic distance. This value has been associated in the literature to be of metavalent bonding character.[34,35,95,96] The intermediate values of $\rho(\vec{r})$ of both bonds, at the BCP and ELF, can be explained by the partial delocalization of electrons of this type of bonding, which stems from the sharing of electrons between several bonds; i.e. there is one single electron per bond instead of two in a typical covalent bond. Therefore, our ELF values support the previous analysis of $\rho(\vec{r})$ and $\nabla^2\rho(\vec{r})$ at the BCP for both interactions. In this way, we have established a new form of identifying metavalent bonds; i.e. they are characterized by an intermediate value of $\rho(\vec{r})$ and a low positive value of $\vec{\nabla}\rho(\vec{r})$. The classification of the different bondings according to $\rho(\vec{r})$, $\nabla^2\rho(\vec{r})$ and ELF are summarized in **Table S3** in SM.

In summary, we conclude that the changes observed both at the Bader and NCI analyses reflect the IPT occurring from the rhombohedral $SnSb_2Te_4$ close to 2 GPa. This IPT is strongly related to the hardening of the Te1-Te1 interlayer interaction and the loss of their predominant vdW character. Moreover, we have shown that Sb-Te1 bonds are polar covalent bonds, whereas the

Sb-Te2 and the Sn-Te2 bonds may fall into what has been recently defined to be the metavalent-type bonding. Finally, we have fully characterized all the bond types present in $SnSb_2Te_4$ by analyzing the electron density. Thus, we have proposed a new method (by using the concepts of $\rho(\vec{r})$ and $\nabla^2\rho(\vec{r})$ at the BCP) to identify the bond character in complex structures, where a coexistence of several types of interactions occurs.

3. Conclusion

Our study of the compressed rhombohedral phase of $SnSb_2Te_4$ at room temperature shows that the rhombohedral phase is stable up to 7 GPa and that a decomposition of the sample occurs above this pressure. This behavior has been framed within the orbital radii map of the tellurium-based ternary chalcogenides (that has been extended) and a possible path at HP has been described for $SnSb_2Te_4$ that can be useful to understand other isostructural compounds of the BA_2Te_4 family.

The compressed rhombohedral structure of $SnSb_2Te_4$ shows an isostructural phase transition above 2 GPa that is mainly caused by a change in the compressibility of the inter-layer space, governed mostly by vdW interactions between the external Te atoms of the *SLs*, which also dominate the behavior of the unit-cell volume under compression. The change in the compressibility of the inter-layer space is clearly reflected on the analysis of the pressure dependence of the calculated electron density topology.

The study of the lattice dynamics of $SnSb_2Te_4$ under compression has allowed us to understand the atomic vibrations of the different phonons and assign the mode symmetries of the Raman-active modes. Furthermore, the description of the atomic vibrations has been compared with their parent binary compounds (c-SnTe and α-Sb_2Te_3). A softening of vibrational modes mainly related to the Sn-Te bonds occurs above 3 GPa, and such a feature has been explained within the framework of the Fermi resonance. Our calculations predict that the Fermi resonance must also be observed in the HP dependence of IR-active modes of parent binary c-SnTe around 2

GPa. Our results show strong correlation between the vibrational modes of $SnSb_2Te_4$ and those of its parent binary compounds. In fact, the Raman spectrum of $SnSb_2Te_4$ shows vibrational modes that are forbidden in c-SnTe; thus showing a novel way to experimentally observe the forbidden vibrational modes of some compounds.

We have also undertaken a study of the pressure dependence of the electrical properties of $SnSb_2Te_4$ with unintentionally p-type semiconducting character in order to verify if an ETT could be observed. The change in the electrical resistance above 8 GPa has been attributed to the sample decomposition; however, a drastic increase in resistance was observed above 2 GPa. This increase has not been attributed to an ETT due to the p-type character of our sample, but to the generation of defects on the ongoing IPT passing from a p-type degenerate to a non-degenerate semiconductor by the reduction of the hole carrier concentration. This result allows the tuning of the electrical properties to improve the TI capabilities of this compound.

Finally, our electron density topology analysis shows that the IPT around 2 GPa is related to the loss of the predominant vdW character by an increment of the ionic character of the interaction between the Te1 atoms of neighbor *SLs*, so the hardening of the Te1-Te1 bond may be the cause of the IPT. The lack of soft phonon branches along the Brillouin zone confirms that the observed IPT is related to a phase transition of higher order than 2; i.e. it is an IPT of electronic origin.

The analysis of the ELF of the Sb-Te1 interaction displays a polar covalent bond character, which remains unalterable under compression. However, the most interesting analysis is obtained when studying the ELF along the Sb-Te2 and Sn-Te interactions, which show the typical intermediate values expected for metavalent bonding. The evaluation of their electronic densities and respective Laplacians at the BCP provides a new criterion to identify these interactions when the material is very complex and different kinds of bonds coexist.

In summary, our study provides new insights into the physics and chemistry of ternary topological insulators of the tetradymite-like ternary BA_2X_4 materials and highlights the

importance of the study of the evolution of the chemical bonds under pressure of topological insulators in order to understand the origin of isostructural phase transitions observed in this family of compounds and the possibility to tune their exceptional properties in a better way than in binary topological insulators.

4. Experimental Section

Sample preparation: Bulk samples were prepared by melting stoichiometric amounts of the pure elements Sn (99.999%, Smart Elements), Sb (99.999%, Smart Elements) and Te (99.999%, Alfa Aesar) at 950 ºC for 93h in sealed silica glass ampoules under argon atmosphere and subsequent annealing at 450 - 500 °C for two days.[31] Representative parts of the samples were crushed to powders and fixed on Mylar foils with silicon grease to collect powder diffraction patterns on a Huber G670 powder diffractometer equipped with an imaging plate detector (Cu-$K_{\alpha 1}$ radiation, Ge monochromator, λ = 1.54051 Å) in Guinier geometry. Rietveld refinement of powder x-ray diffraction data confirmed the high purity of the samples.

Theoretical Calculations: *Ab-initio* calculations have been performed within the density functional theory (DFT)[97] using plane-wave basis-sets and the projector-augmented wave (PAW)[98] scheme with the Vienna *Ab-initio* Simulation Package (VASP) package.[99] Calculations of the electronic-band structures have been considered by employing spin-orbit coupling (SOC). The plane-wave kinetic-energy cutoff was defined with 320 eV, in order to achieve highly converged results. We have used the generalized-gradient approximation (GGA) for the exchange-correlation energy with the Perdew-Burke-Ernzerhof parameterization revised for solids (PBEsol).[100] At each selected volume, the structures were fully relaxed to their equilibrium configuration through the calculation of the forces on atoms and the stress tensor with a dense special k-point sampling Monkhorst-Pack grids. In particular, the electronic band structures along high-symmetry directions and the

corresponding electronic density of states (EDOS) were computed with a mesh of 18x18x18 k-points. The application of DFT-based calculations to the study of semiconductor properties under HP has been reviewed in the literature.[101]

Lattice-dynamics calculations of phonon modes were performed at the zone center (Γ point) of the Brillouin zone. For the calculation of the dynamical matrix at Γ we used the direct force-constant approach (or supercell method),[99,102] which involves the calculation of all the atomic forces when each non-symmetry related atom in the unit cell is displaced along non-symmetry related directions.

The Bader analysis was performed by partitioning the PBEsol-DFT core and valance charge density grids.[103-107] A fine FFT grid was required to accurately reproduce the correct total core charge. The Non-Covalent Interactions (NCI) of the PBEsol-DFT charge densities was computed using the NCIPLOT tool.[91,92] Such a tool defines a visualization index based on the electron density and its derivatives, enabling identification of non-covalent interactions, based on the peaks that appear in the reduced density gradient at low densities.

Synchrotron based angle-dispersive X-ray diffraction (ADXRD) under pressure experiments: HP-ADXRD measurements on $SnSb_2Te_4$ at 300 K using a membrane-type diamond-anvil cell (DAC) were carried out in experiment 1 (experiment 2) up to 37 GPa (12 GPa) in beamline I15 (MSPD beamline[108]) at Diamond Light Source synchrotron (ALBA synchrotron) using a monochromatic X-ray beam with λ = 0.42408 Å (λ = 0.4246 Å). In experiment 1 (experiment 2) images were collected using a MAR345 image plate (Rayonix MARCCD detector) located at 430 mm (240 mm) from the sample. In experiment 1 (experiment 2), $SnSb_2Te_4$ powder was loaded in a 150-μm diameter hole of a Rhenium (Inconel) gasket in a DAC with diamond-culet sizes of 350 μm using helium (silicone oil) as pressure transmitting medium (PTM). In both experiments, copper was placed inside the pressure cavity and used as the pressure sensor through copper EoS[109] and a pinhole placed before the sample position was used as a

clean-up aperture for filtering out the tail of the X-ray beam, which was focused down to 20 x 20 μm^2 using Kickpatrick-Baez mirrors.

Diffraction patterns obtained in both experiments were integrated as a function of 2θ using FIT2D software in order to give conventional, one-dimensional diffraction profiles.[110] The refinement of the powder diffraction patterns was performed using GSAS program package.[111,112] Due to the resonant excitation energy with Sn K-edge used in both experiments, the relative intensities are not accurate enough to perform Rietveld refinement but a Von Dreele-type Le Bail fit. Therefore, all the experimental structural parameters presented in this work have been obtained by means of a Von Dreele-type Le Bail method. Unfortunately, the lack of Rietveld refinement in our measurements prevents us from validating the degree of cation mixing in our samples.

Raman scattering (RS) measurements under pressure: Unpolarized HP-RS measurements up to 27 GPa using a membrane-type DAC and 16:3:1 methanol/ethanol/water mixture as PTM (quasi-hydrostatic up to 10 GPa),[113,114] were performed with a Horiba Jobin Yvon LabRAM UV HR microspectrometer equipped with a thermoelectrically cooled multichannel charge coupled device detector which allows a spectral resolution better than 2 cm^{-1}. The Raman signal was excited with a He-Ne laser (632.8 nm line) with a power of less than 10 mW and collected in backscattering geometry using an edge filter working in perpendicular configuration and cutting at 100 cm^{-1}. Raman signals down to 50 cm^{-1} can eventually be detected by adjusting the angle between the edge filter and the light containing the Raman signal (provided that the Rayleigh signal is weak enough and the Raman signal is strong enough). Pressure was determined by the ruby luminescence method. The frequency of the Raman-active phonons has been experimentally analyzed by fitting Raman peaks with a Voigt profile fixing the Gaussian line width (1.6 cm^{-1}) to the experimental setup resolution.[117,118]

Transport properties under pressure: Electrical resistance of $SnSb_2Te_4$ under pressure was measured with the standard four-point probe van der Pauw method using 20 μm copper-

beryllium wires. Single crystals of $SnSb_2Te_4$ of approx. 30 μm thick and 100 x 100 μm^2 surface were loaded into a Merrill-Bassett DAC with 400 μm culet diamonds. The electrical average resistance was measured by using four 20 μm copper-beryllium wires. Electrical resistance was measured under two different arrangements. In the first one, the sample was directly in contact with the anvils; i.e. under non-hydrostatic conditions. In the second one, the sample was inside a stainless steel gasket and surrounded by CsI powder as PTM; i.e. under quasi-hydrostatic conditions. Electrical resistance showed similar trends in both arrangements, likely due to the anisotropic (layered) and soft nature of the crystals. Luminescence lines of Ruby powder were used to calibrate the pressure inside the cavity in both methods.[115,116]

Supporting Information
Supporting Information is available from the Wiley Online Library or from the author.

Acknowledgements
This work has been performed under financial support from Spanish MINECO under projects MALTA Consolider Ingenio 2010 network (MAT2015-71070-REDC) and projects FIS2017-83295-P and MAT2016-75586-C4-1/2/3-P, from Generalitat Valenciana under project PROMETEO/2018/123. This publication is fruit of "Programa de Valoración y Recursos Conjuntos de I+D+i VLC/CAMPUS and has been financed by the Spanish Ministerio de Educación, Cultura y Deporte as part of "Programa Campus de Excelencia Internacional". Supercomputer time has been provided by the Red Española de Supercomputación (RES) and the MALTA cluster. JAS acknowledges "Ramón y Cajal" fellowship (RYC-2015-17482) program for financial support and ELdS acknowledges Marie Sklodowska-Curie grant No. 785789-COMEX from European Union's Horizon 2020 research and innovation programme. We also thank ALBA synchrotron and DIAMOND light source for funded experiments.

Received: ((will be filled in by the editorial staff))
Revised: ((will be filled in by the editorial staff))
Published online: ((will be filled in by the editorial staff))

References

[1] A. R. Mellnik, J. S. Lee, A. Richardella, J. L.Grab, P. J. Mintun, M. H. Fischer, A. Vaezi, A. Manchon, E.-A. Kim, N. Samarth, D. C. Ralph. *Nature* **2014**, 511, 449.

[2] Y. L. Chen, J. G. Analytis, J.-H. Chu, Z. K. Liu, S.-K. Mo, X. L. Qi, H. J. Zhang, D. H. Lu, X. Dai, Z. Fang, S. C. Zhang, I. R. Fisher,Z. Hussain, Z.-X. Shen. *Science* **2009**, 325, 178.

[3] D. Hsieh, Y. Xia, D. Qian, L. Wray, J. H. Dil, F. Meier, J. Osterwalder, L. Patthey, J. G. Checkelsky, N. P. Ong, A. V. Fedorov, H. Lin, A. Bansil, D. Grauer, Y. S. Hor, R. J. Cava, M. Z. Hasan. *Nature* **2009**, 460, 1101.

[4] T. Zhang, Y. Jiang, Z. Song, H. Huang, Y. He, Z. Fang, H. Weng, C. Fang. *Nature* **2019**, 566, 475.

[5] M. G. Vergniory, L. Elcoro, C. Felser, N. Regnault, B. Andrei Bernevig, Z. Wang. *Nature* **2019**, 566, 480.

[6] F. Tang, H. C. Po, A. Vishwanath, X. Wan. *Nature* **2019**, 566, 486.

[7] A. Zunger. *Nature* **2019**, 566, 447.

[8] H. Zhang, C.X. Liu, X.L. Qi, X. Dai, Z. Fang, S.-C. Zhang. *Nature Physics* **2009**, 5, 438.

[9] Y. Xia, D. Qian, D. Hsieh, L. Wray, A. Pal, H. Lin, A. Bansil, D. Grauer, Y. S. Hor, R. J. Cava, M. Z. Hasan. *Nature Physics* **2009**, 5, 398.

[10] M. Taherinejad, K. F. Garrity, D. Vanderbilt. *Phys. Rev. B* **2014**, 89, 115102.

[11] D. Niesner, S. Otto, V. Hermann, Th. Fauster, T. V. Menshchikova, S. V. Eremeev, Z. S. Aliev, I. R. Amiraslanov, M. B. Babanly, P. M. Echenique, and E. V. Chulkov. *Phys. Rev. B* **2014**, 89, 081404(R).

[12] D.M. Rowe, *CRC Handbook of Thermoelectrics*, CRC Press Inc., New York, **1995**.

[13] R. Venkatasubramanian, E. Siivola, T. Colpitts, B. O'Quinn. *Nature* **2001**, 413, 597.

[14] S.V. Eremeev, Y.M. Koroteev, E.V. Chulkov. *JETP Letters* **2010**, 91, 387.

[15] T.V. Menshchikova, S.V. Eremeev, E.V. Chulkov. *JETP Letters* **2011**, 94, 106.

[16] T.V. Menshchikova, S.V. Eremeev, E.V. Chulkov. *Appl. Surf. Sci.* **2013**, 267, 1.

[17] G. Concas, T.M. de Pascale, L. Garbato, F. Ledda, F. Meloni, A. Rucci, M. Serra. *J. Phys, Chem. Solids* **1992**, 53, 79.

[18] S. V. Eremev, T. V. Menschikova, I. V. Silkin, M. G. Vergniory, P. M. Echenique, E. V. Chulkov. *Phys. Rev. B* **2015**, 91, 245145.

[19] K. A. Agaev, A. G. Talybov. *Kristallografiya* **1966**, 11, 454.

[20] R. M. Imamov, S. A. Semiletov, and Z. G. Pinsker. *Soviet Phys. Cryst.* **1970**, 15, 239.

[21] A. Y. Kuznetsov, A. S. Pereira, A. A. Shiryaev, J. Haines, L. Dubrovinsky, V. Dmitriev, P. Pattison, N. Guignot. *J. Phys. Chem. B* **2006**, 110, 13858.

[22] L.E. Shelimova, O.G. Karpinskii, P.P. Konstantinov, E.S. Avilov, M.A. Kretova and V.S. Zemskov. *Inorg. Mater.* **2004**, 40, 451.

[23] B. A. Kuropatwa, A. Assoud, H. Kleinke. Z. Anorg. Allg. Chem. **2013**, 639, 2411.

[24] B. A. Kuropatwa, H. Kleinke. Z. Anorg. Allg. Chem. **2012**, 638, 2640.

[25] A. Banik, and K. Biswas. *Angew. Chem. Int. Ed.* **2017**, 56, 14561.

[26] L.E. Shelimova, O.G. Karpinskii, T.E. Svechnikova, I.Y. Nikhezina, E.S. Avilov, M.A. Kretova, V.S. Zemskov. *Inorg. Mater.* **2008**, 44, 371.

[27] H.W. Shu, S. Jaulmes, J. Flahaut. *J. Solid State Chem.* **1988**, 74, 277.

[28] T.B. Zhukova, A.I. Zaslavskii. *Sov. Phys. Crystallogr.* **1972**, 16, 796.

[29] K. Adouby, A. A. Toure, G. Kra, J. Olivier-Fourcade, J. C. Jumas, C. P. Vicente. *C. R. Acad. Sci., Chem.* **2000**, 3, 51.

[30] T.B. Zhukova, A.I. Zaslavskii. *Kristallografiya* **1971**, 16, 918.

[31] O. Oeckler, M. N. Schneider, F. Fahrnbauer, G. Vaughan. *Sol. State Sci.* **2011**, 13, 1157.

[32] T. Schafer, P. M. Konze, J. D. Huyeng, V. L. Deringer, T. Lesieur, P. Muller, M. Morgenstern, R. Dronkowski and M. Wuttig. *Chem. Mater.* **2017**, 29, 6749.

[33] J. Gallus. Diplomarbeit, Rheinisch-Westfälischen Technischen Hochschule Aachen, 2011.

[34] M. Wuttig, V. L. Deringer, X. Gonze, C. Bichara, J. Y. Raty. *Adv. Mater.* **2018**, 30, 1803777.

[35] J.Y. Raty, M. Schumacher, P. Golub, V. L. Deringer, C. Gatti and M. Wuttig. *Adv. Mater.* **2019**, 31, 1806280.

[36] Y. Yu, M. Cagnoni, O. Cojocaru-Mirédin, M. Wuttig. *Adv. Funct. Mater.* **2019**, 30, 1904862.

[37] Y. Cheng, O. Cojocaru-Mirédin, J. Keutgen, Y. Yu, M. Küpers, M. Schumacher, P. Golub, J.-Y. Raty, R. Dronskowski, and M. Wuttig. *Adv. Mat.* **2019**, 31, 1904316.

[38] W.-P. Hsieh, P. Zalden, M. Wuttig, A. M. Lindenberg, W. L. Mao. *Appl. Phys. Lett.* **2013**, 103, 191908.

[39] R. Vilaplana, J. A. Sans, F. J. Manjón, J. Sánchez-Benítez, C. Popescu, O. Gomis, A. L. J Pereira, B. García-Domene, P. Rodríguez-Hernández, A. Muñoz, D. Daisenberger, O. Oeckler. J. All. Comp. **2016**, 685, 962.

[40] P. Song, R. Matsumoto, Z. Hou, S. Adachi, H. Hara, Y. Saito, P. B. Castro, H. Takeya, Y. Takano. *J. Phys. Condens. Matter.* **2020**, 32, 235901.

[41] R. J. Angel, J. Gonzalez-Platas, M. Alvaro. *Z. Kristall.* **2014**, 229, 405.

[42] D. Zhou, Q. Li, Y. Ma, Q. Cui, C. Chen. *J. Phys. Chem. C* **2013**, 117, 5352.

[43] O. Gomis, R. Vilaplana, F. J. Manjón, P. Rodríguez-Hernández, E. Pérez-González, A. Muñoz. V. Kucek, C. Drasar. *Phys. Rev. B* **2011**, 84, 174305.

[44] N. Sakai, T. Kajiwara, K. Takemura, S. Minomura, Y. Fujii. *Sol. State Comm.* **1981**, 40, 1045.

[45] B.-T. Wang, P. Souvatzis, O. Eriksson, P. Zhang. *J. Chem. Phys.* **2015**, 142, 174702.

[46] A. L. J. Pereira, J. A. Sans, R. Vilaplana, O. Gomis, F. J. Manjon, P. Rodríguez-Hernandez, A. Muñoz, C. Popescu, A. Beltran. *J. Phys. Chem. C* **2014**, 118, 23189.

[47] V.P. Cuenca-Gotor, J.A. Sans, J. Ibáñez, C. Popescu, O. Gomis, R. Vilaplana, F.J. Manjón, A. Leonardo, E. Sagasta, A. Suárez-Alcubilla, I.G. Gurtubay, M. Mollar, and A. Bergara. *J. Phys. Chem. C* **2016**, 120, 19340.

[48] K. Robinson, G. V. Gibbs, P. H. Ribbe. *Science* **1971**, 172, 567.

[49] W. H. Baur. *Acta Crystallogr., Sect. B: Struct. Sci.* **1974**, 30, 1195.

[50] A. Walsh, and W. Watson. *J. Phys. Chem. B* **2005**, 109, 18868.

[51] A. Skowron, F. W. Boswell, J. M. Corbett, N. J. Taylor. J. Sol. Stat. Chem. **1994**, 112, 251.

[52] P. K. Smith, J. B. Parise. *Acta Cryst.* **1985**, B41, 84.

[53] Y. Iitaka, W. Nowacki. *Acta Cryst.* **1962**, 15, 691.

[54] X. Zhang, V. Stevanović, M. d'Avezac, S. Lany, A. Zunger. *Phys. Rev. B* **2012**, 86, 014109.

[55] A. Zunger. *Phys. Rev. B* **1980**, 22, 5839.

[56] F. J. Manjón, R. Vilaplana, O. Gomis, E. Pérez-González, D. Santamaría-Pérez, V. Marín-Borrás, A. Segura, J. González, P. Rodríguez-Hernández, A.Muñoz, C. Drasar, V. Kucek, and V. Muñoz-Sanjosé. *Phys. Stat. Sol. (b)* **2013**, 250, 669.

[57] A. V. Kolobov, J. Haines, A. Pradel, M. Ribes, P. Fons, J. Tominaga, Y. Katayama, T. Hammouda, and T. Uruga. *Phys. Rev. Lett.* **2006**, 97, 035701.

[58] A. K. Arora. *Sol. State Comm.* **2000**, 115, 665.

[59] W. A. Basset, L.-C. Ming. *Phys. Earth Planet. Interiors* **1972**, 6, 154.

[60] Y. Fei, H.-K. Mao. *J. Geophys. Res.* **1993**, 98, 11875.

[61] A. Y. Kuznetsov, A. S. Pereira, A. A. Shiryaev, J. Haines, L. Dubrovinsky, V. Dmitriev, P. Pattison, N. Guignot. *J. Phys. Chem. B* **2006**, 110, 13858.

[62] J. Catafesta, P. R. Rovani, C. A. Perottoni, A. S. Pereira. *J. Phys. Chem. Sol.* **2015**, 77, 151.

[63] D. Duan, X. Huang, F. Tian, D. Li, H. Yu, Y. Liu, Y. Ma, B. Liu, and T. Cui. *Phys. Rev. B* **2015**, 91, 180502(R).

[64] J. Zhu, J. L. Zhang, P. P. Kong, S. J. Zhang, X. H. Yu, J. L Zhu, Q. Q. Liu, X. Li, R. C. Yu, R. Ahuja, W. G. Yang, G. Y. Shen, H. K. Mao, H. M. Weng, X. Dai, Z. Fang, Y. S. Zhao, C. Q. Jin. *Scientific Reports* **2013**, 3, 2016.

[65] L. Zhao, H. Deng, I. Korzhovska, M. Begliarbekov, Z. Chen, E. Andrade, E. Rosenthal, A. Pasupathy, V. Oganesyan, L. Krusin-Elbaum. *Nat. Comm.* **2015**, 6, 8279.

[66] E. Kroumova, M. I. Aroyo, J. M. Perez Mato, A. Kirov, C. Capillas, S. Ivantchev, H. Wondratschek. *Phase Trans.* **2003**, 76, 155.

[67] P. Canepa, R. M. Hanson, P. Ugliengo, M. Alfredsson. *J. Appl. Cryst.* **2011**, 44, 225.

[68] C. Marini, D. Chermisi, M. Lavagnini, D. Di Castro, C. Petrillo, L. Degiorgi, S. Scandolo, P. Postorino. *Physical Review B* **2012**, 86, 064103.

[69] R. Vilaplana, O. Gomis, E. Pérez-González, H.M. Ortiz, F.J. Manjón, P. Rodríguez-Hernández, A. Muñoz, P. Alonso-Gutiérrez, M.L. Sanjuán, V.V. Ursaki and I.M. Tiginyanu. *J. Phys. Chem. C* **2013**, 117, 15773.

[70] G.A.S. Ribeiro, L. Paulatto, R. Bianco, I. Errea, F. Mauri, and M. Calandra. *Phys. Rev. B* **2018**, 97, 014306.

[71] J. Pellicer-Porres, A. Segura, Ch. Ferrer-Roca, J. A. Sans, P. Dumas. *J. Phys.: Condens. Matter.* **2013**, 25, 505902.

[72] C.-H. Wang, X.-P. Jing, W. Feng, J. Lu. *J. Appl. Phys.* **2008**, 104, 034112.

[73] K. Zhao, Y. Wang, Y. Sui, C. Xin, X. Wang, Y. Wang, Z. Liu, and B. Li. *Phys. Status Solidi RRL* **2015**, 9, 379.

[74] B.-T. Wang, P. Souvatzis, O. Eriksson, and P. Zhang. *J. Chem. Phys.* **2015**, 142, 174702.

[75] M. Cardona, M. L. Thewalt. *Rev. Mod. Phys.* **2005**, 77, 1173.

[76] F. J. Manjón, J. Serrano, I. Loa, K. Syassen, C. T. Lin, M. Cardona. *Phys. Stat. Sol. (B)* **2001**, 223, 331.

[77] M. Krauzman, R. M. Pick, H. Poulet, G. Hamel, B. Prevot. *Phys. Rev. Lett.* **1974**, 33, 528.

[78] G. Kanellis, W. Kress, H. Bilz. *Phys. Rev. Lett.* **1986**, 56, 938.

[79] V. M. Agranovich, *Spectroscopy and Excitation Dynamics of Condensed Moiecular Systems*. Edited by North-Holland, Amsterdam, **1983**, 83.

[80] M. A. Hakeem, D. E. Jackson, J. J. Hamlin, D. Errandonea, J. E. Proctor, and M. Bettinelli. *Inorg. Chem.* **2018**, 57, 7550.

[81] N. Sakai, T. Kajiwara, K. Takemura, S. Minomura, and Y. Fujii. *Sol. State Comm.* **1981**, 40, 1045.

[82] D. Errandonea, A. Segura, D. Martínez-García and V. Muñoz-San Jose. *Phys. Rev. B* **2009**, 79, 125203.

[83] A. Segura, V. Panchal, J.F. Sánchez-Royo, V. Marín-Borrás, V. Muñoz-Sanjosé, P. Rodríguez-Hernández, A. Muñoz, E. Pérez-González, F.J. Manjón, and J. González. *Phys. Rev. B* **2012**, 85, 195139.

[84] A. M. Mio, P. M. Konze, A. Meledin, M. Küpers, M. Pohlmann, M. Kaminski, R. Dronskowski, J. Mayer, M. Wuttig. *Adv. Funct. Mat.* **2019**, 29, 1902332.

[85] S. Noury, B. Silvi. *Inorg. Chem.* **2002**, 41, 2164.

[86] S. Scheiner, J. Lu. *Chem. Eur. J.* **2018**, 24, 8167.

[87] M. C. Durrant. *Chem. Sci.* **2015**, 6, 6614.

[88] B. Braida, P. C. Hilberty. Nat. Chem. **2013**, 5, 417.

[89] T. H. Lee, S. R. Elliott. arXiv:1909.05281

[90] S. Shaik, D. Danovich, J. M. Galbraith, B. Braïda,W. Wu, and P. C. Hiberty. *Angew. Chem. Int. Ed.* **2019**, 58, 2.

[91] E. R. Johnson, S. Keinan, P. Mori-Sanchez, J. Contreras-Garcia, A. J. Cohen, and W. Yang. *J. Am. Chem. Soc.* **2010**, 132, 6498.

[92] J. Contreras-Garcia, E. R. Johnson, S. Keinan, R. Chaudret, J-P. Piquemal, D. N. Beratan, and W. Yang. *J. Chem. Theory Comput.* **2011**, 7, 625.

[93] S. Berski, P. Durlak. *Polyhedron* **2017**, 129, 22.

[94] C. Gatti. *Z. Kristallogr.* **2005**, 220, 390.

[95] M. Xu, S. Jakobs, R. Mazzarello, J.-Y. Cho, Z. Yang, H. Hollermann, D. Shang, X.S. Miao, Z.H. Yu, L. Wang, and M. Wuttig. *J. Phys. Chem. C* **2017**, 121, 25447.

[96] V. P. Cuenca-Gotor, J. A. Sans, O. Gomis, A. Mujica, S. Radescu, A. Muñz, P. Rodríguez-Hernández, E. Lora da Silva, C. Popescu, Jordi Ibáñez, R. Vilaplana and F. J. Manjón. *Phys. Chem. Chem. Phys.* **2020**, 22, 3352.

[97] P. Hohenberg W. Kohn. *Phys. Rev. B* **1964**, 136, 864.

[98] P. E. Blöchl. *Phys. Rev. B* **1994**, 50, 17953.

[99] G. Kresse, J. Hafner. *Phys. Rev. B* **1993**, 47, 558.

[100] J. P. Perdew, A. Ruzsinszky, G. I. Csonka, O. A. Vydrow, G. E. Suseria, L. A. Constantin, X. Zhou, K. Burke. *Phys. Rev. Lett.* **2008**, 100, 136406.

[101] A. Mujica, A. Rubio, A. Muñoz, R. J. Needs. *Rev. Mod. Phys.* **2003**, 79, 863.

[102] K. Parlinski, see: *http://www.computingformaterials.com/index.html*. March 2020.

[103] W. Tang, E. Sanville, and G. Henkelman. *J. Phys.: Compute Mater.* **2009**, 21, 084204.

[104] E. Sanville, S. D. Kenny, R. Smith, and G. Henkelman. *J. Comp. Chem.* **2007**, 28, 899.

[105] G. Henkelman, A. Arnaldsson, and H. Jónsson. *Comput. Mater. Sci.* **2006**, 36, 254.

[106] M. Yu and D. R. Trinkle. *J. Chem. Phys.* **2011**, 134, 064111.

[107] http://theory.cm.utexas.edu/henkelman/code/bader/. March 2019

[108] F. Fauth, I. Peral, C. Popescu, M. Knapp. *Powder Diffr.* **2013**, 28, 360.

[109] A. Dewaele, P. Loubeyre, M. Mezouar. *Phys. Rev. B* **2004**, 70, 094112.

[110] A. P. Hammersley, S. O. Svensson, M. Hanfland, A. N. Fitch, D. Häusermann. *High Press. Res.* **1996**, 14, 235.

[111] B. H. Toby. *J. Appl. Crystallogr.* **2001**, 34, 210.

[112] A. C. Larson, R. B. Von Dreele. *Los Alamos National Laboratory Report LAUR* **1994**, 86, 748.

[113] S. Klotz, J.-C. Chervin, P. Munsch and G. Le Marchand. *J. Phys. D: Appl. Phys.* **2009**, 42, 075413.

[114] D. Errandonea, A. Muñoz, J. González-Platas. *J. Appl. Phys.* **2014**, 115, 216101.

[115] H. K. Mao, J. Xu, P. M. Bell. *J. Geophys. Res.* **1986**, 91, 4673.

[116] K. Syassen. *High Press. Res.* **2008**, 28, 75.

[117] A. Debernardi, C. Urlich, M. Cardona, K. Syassen. *Phys. Stat. Solid. (b)* **2001**, 223, 213.

[118] B. García-Domene, H. M. Ortiz, O. Gomis, J. A. Sans, F. J. Manjón, A. Munoz, P. Rodríguez-Hernández, S. N. Achary, D. Errandonea, D. Martínez-García, A. H. Romero, A. Singhal, A. K. Tyagi. *J. Appl. Phys.* **2012**, 112, 123511.

[119] T. Matsunaga and N. Yamada. *Phys. Rev. B* **2004**, 69, 104111.

[120] O. G. Karpinskii, L. E. Shelimova, M. A. Kretova. *Inorg. Mat.* **1997**, 33, 793.

[121] L. E. Shelimova, O. G. Karpinskii, T. E. Svechnikova, I. Y. Nikezhina, E. S. Avilov, M. A. Kretova, V. S. Zemskov. *Neorg. Mater.* **2008**, 44, 438.

[122] K. A. Agaev, S. A. Semiletov. *Kristallografiya* **1968**, 13, 258.

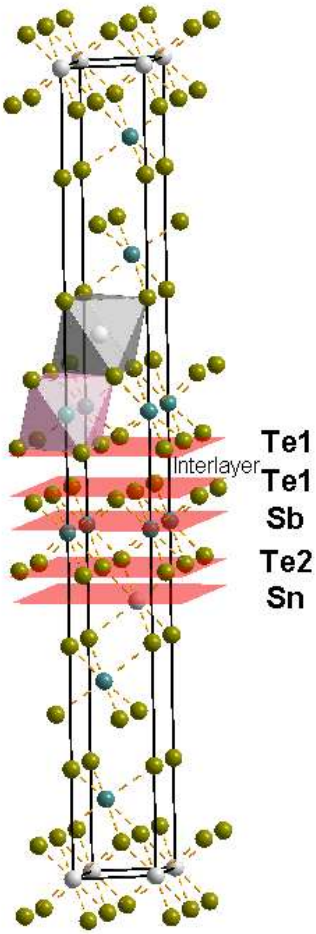

Figure 1. 3D structure layout of the $SnSb_2Te_4$ compound. Atomic planes are defined.

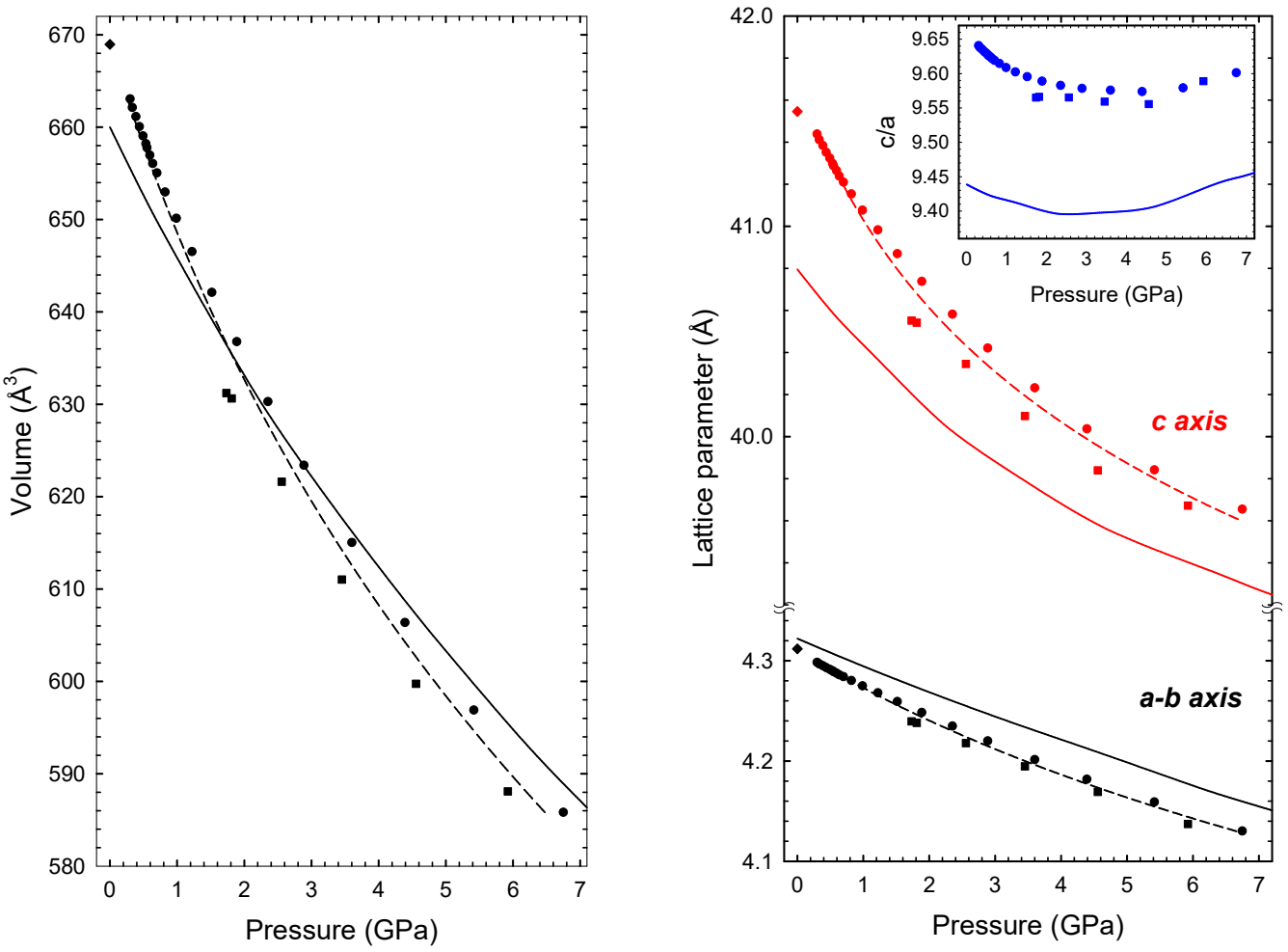

Figure 2. Pressure dependence of the unit cell volume (a) and lattice parameters (b). The inset shows the evolution of the c/a ratio with pressure. Solid lines represent the theoretically simulated data, dashed lines represents the fit to EoS equations, solid circles are the experimental data obtained using silicone oil as PTM and solid squares are the experimental data obtained using helium as PTM.

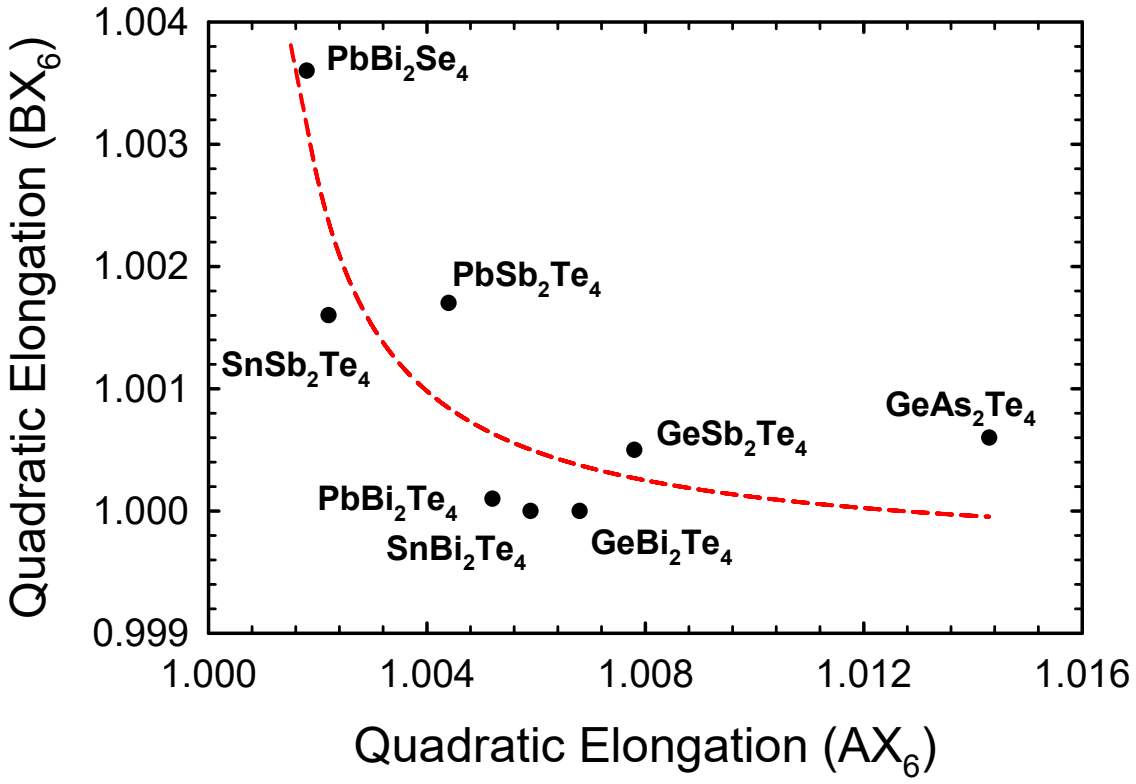

Figure 3. Relationship between the quadratic elongation of the BX_6 octahedron and the quadratic elongation of the AX_6 octahedron in AB_2X_4 materials. Structures obtained from Refs. **[27,28,119-122]**

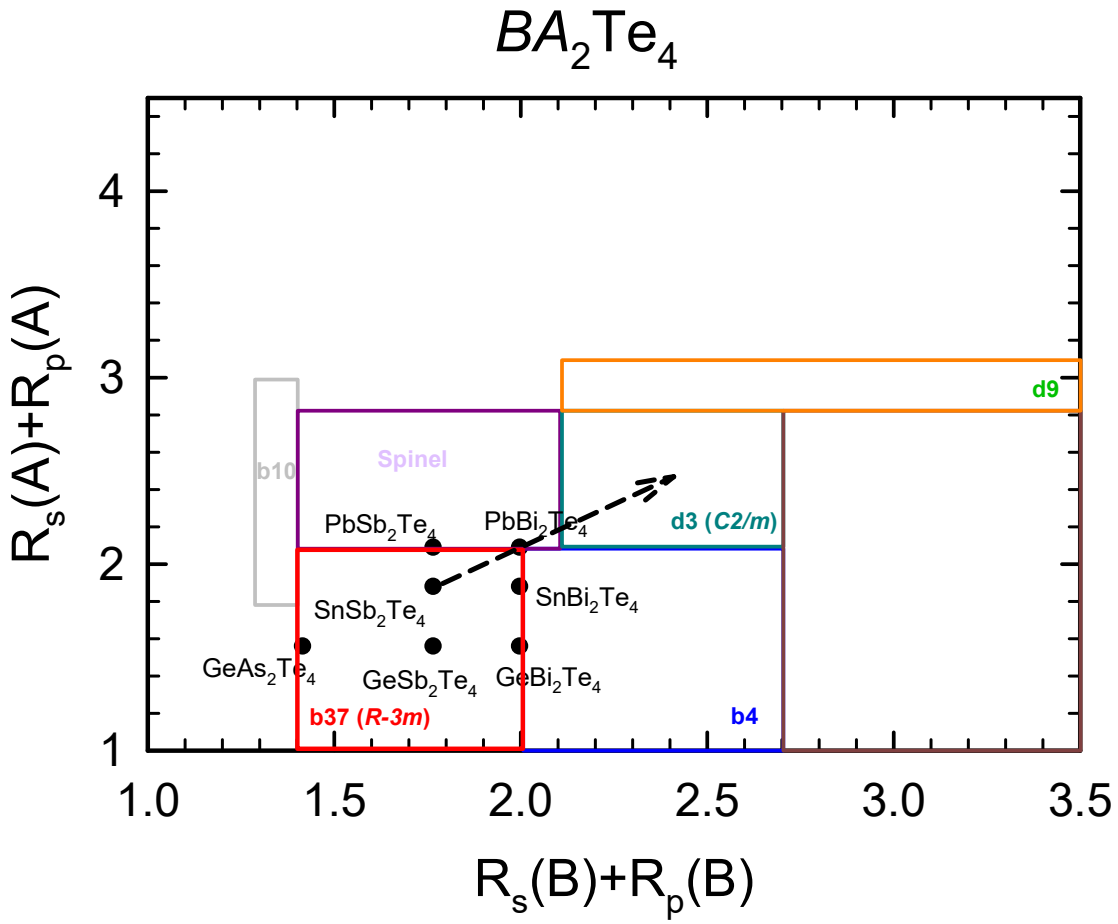

Figure 4. Updated orbital radii map of stable *BA_2Te_4* compounds initially proposed by Zhang et al. **[54]**

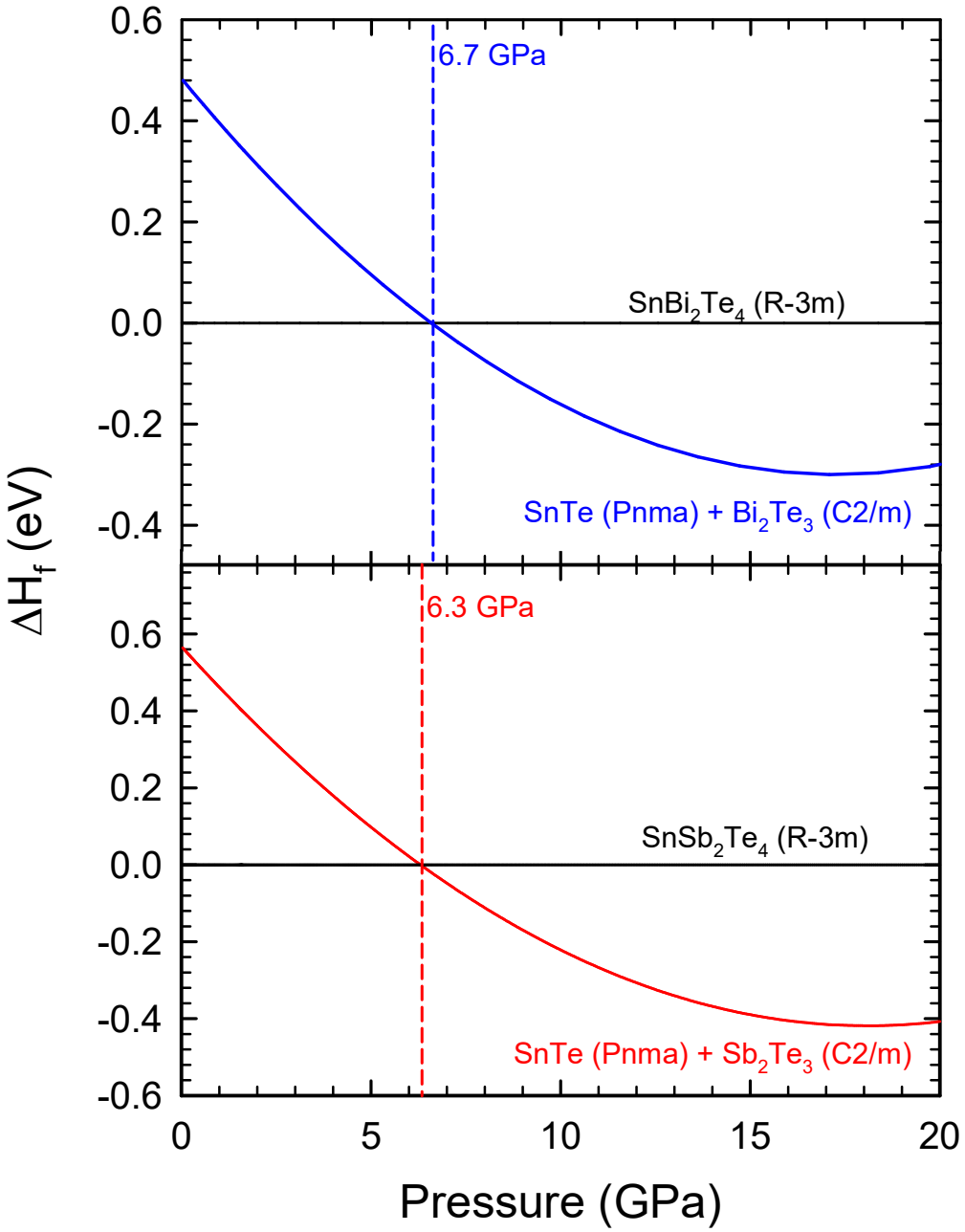

Figure 5. Relative formation enthalpy of the HP phases of the parent binary compounds with respect to the $R\bar{3}m$ structure of $SnSb_2Te_4$ and $SnBi_2Te_4$.

Figure 6.

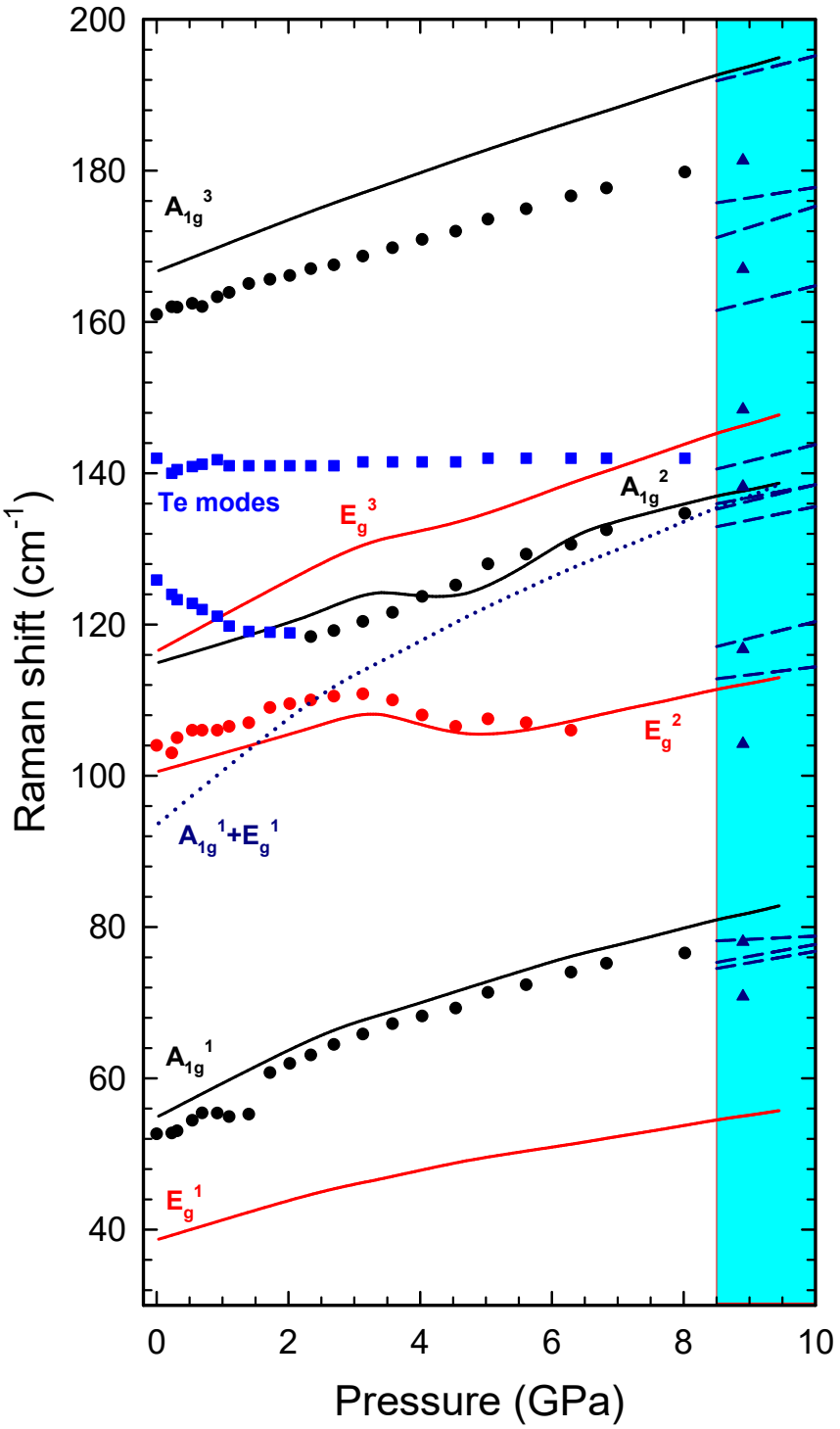

Pressure dependence of the experimental (symbols) and theoretical (lines) Raman-active mode frequencies in $SnSb_2Te_4$. Dotted line represents the pressure dependence of the $A_{1g}^1 + E_g^1$ combination at Γ, while dashed lines represent the Raman-active modes expected for β-Sb_2Te_3.

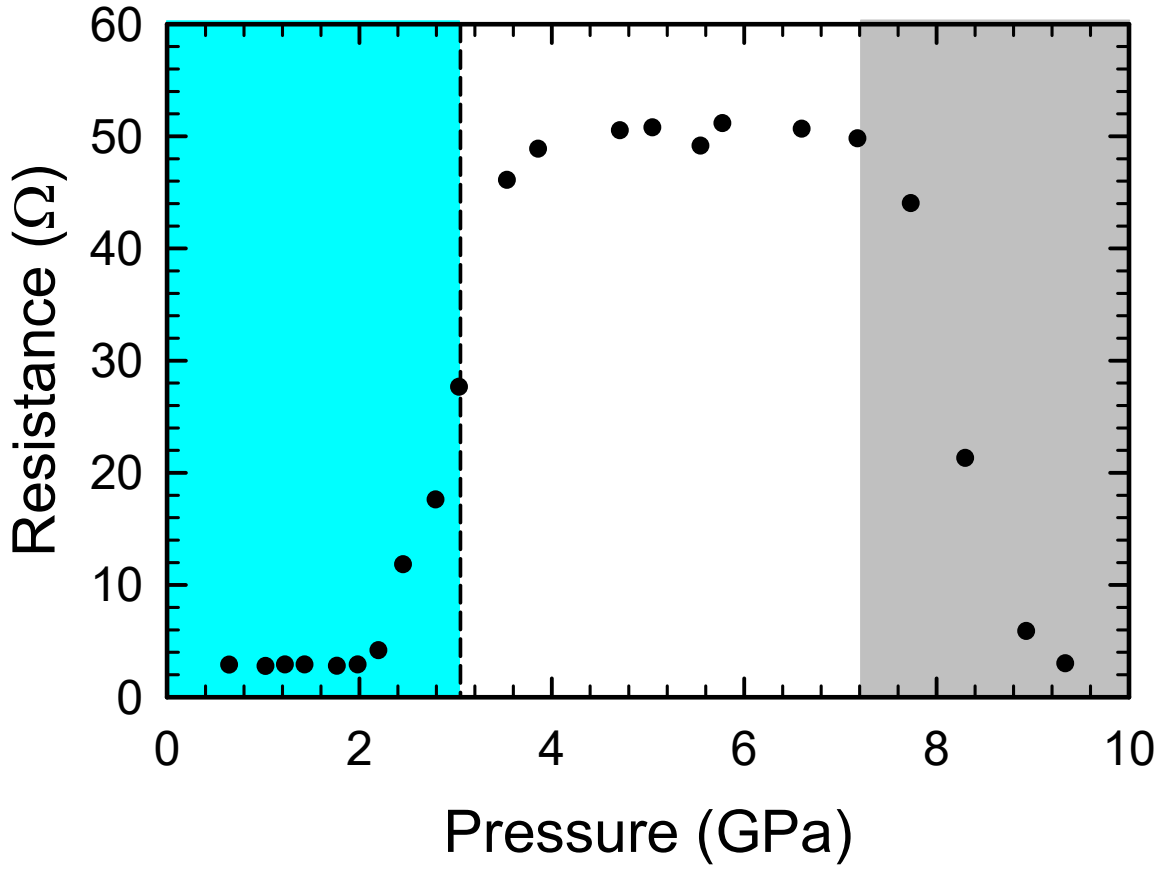

Figure 7. Evolution of the resistance of compressed $SnSb_2Te_4$ recorded during the upstroke.

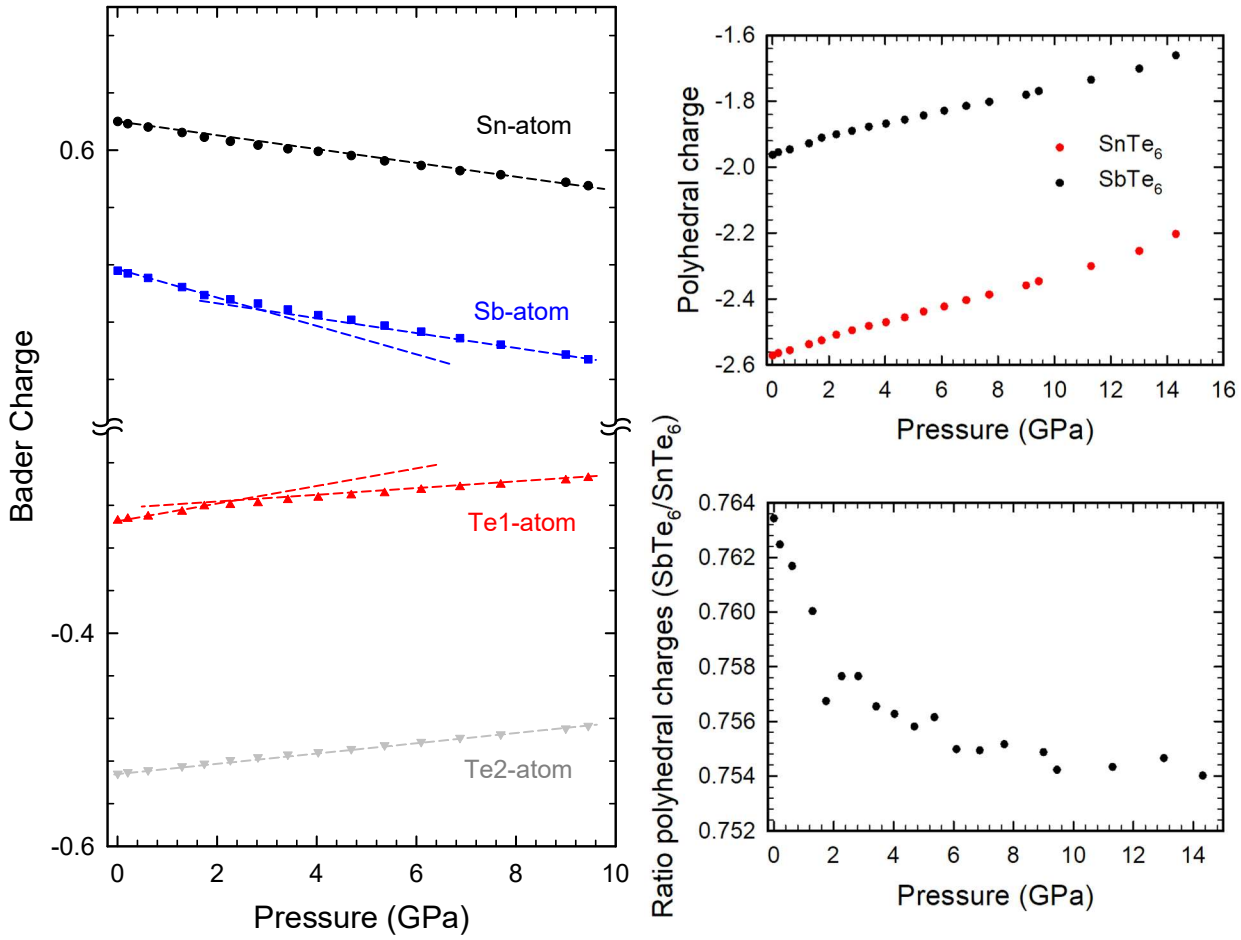

Figure 8. Evolution of the (a) Bader charge of the different crystallographic atoms under pressure and (b) the ratio between Te1/Te2 and (c) Sn/Sb Bader charge.

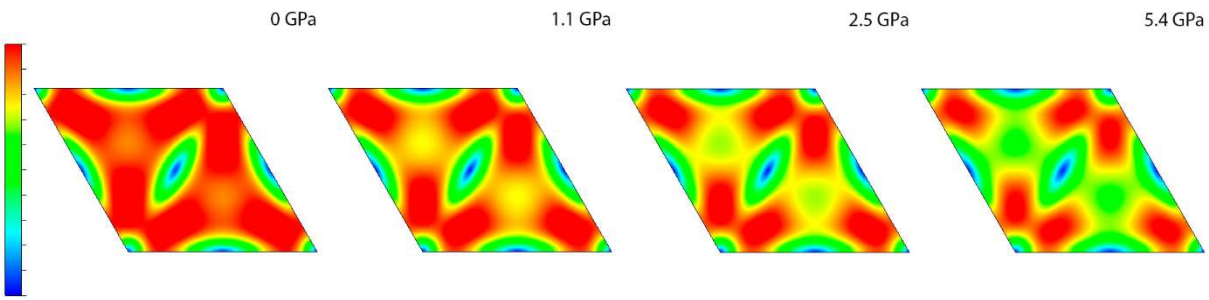

Figure 9. Evolution of the electronic distribution in the interlayer plane with increasing pressure.

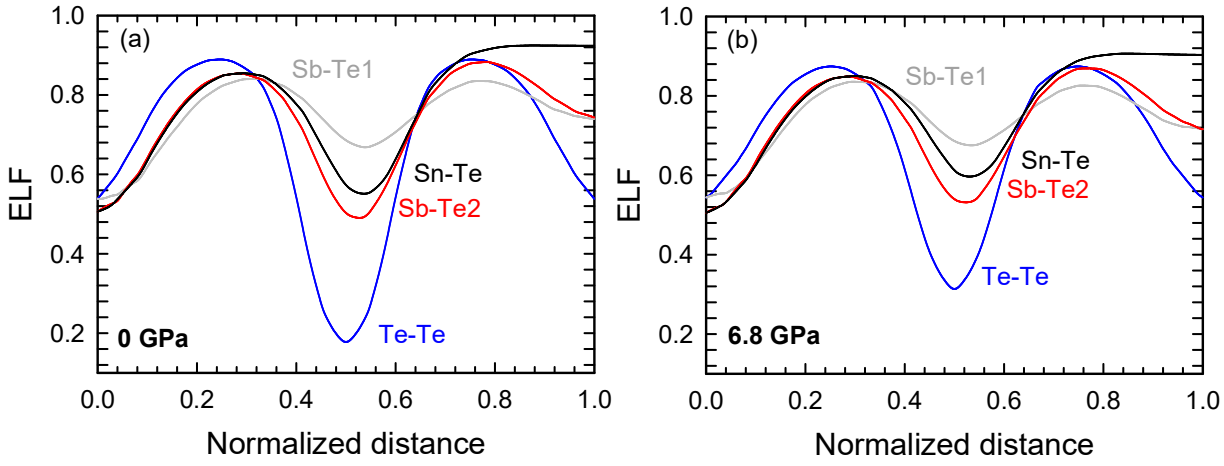

Figure 10. Pressure dependence of the ELF along the path of the Sb-Te1, Sb-Te2, Sn-Te and Te-Te bonds at 0 GPa **(a)** and 6.8 GPa **(b)**.

Table 1. Calculated (th.) and experimental (exp.) Volume (V_0), bulk modulus (B_0), and its derivative (B_0') of $SnBi_2Te_4$ and $SnSb_2Te_4$ at ambient pressure.

	V_0 (Å^3)	B_0 (GPa)	B_0'
	$SnSb_2Te_4$		
exp.[a]	663.1(6)	31.6(14)	8(8)
th.(GGA-PBESol)[b]	659.3(6)	41.0(15)	6.5(6)
	α-Sb_2Te_3		
exp.[c]	481.1(8)	36.1(9)	6.2(4)
th.(GGA-PBESol)[d]	473.1(8)	43(2)	4.3(5)

[a)] This work; [b)] Calculations including SOC in this work; [c)] Average experimental value from Ref. 43; [d)] Calculations including SOC from Ref. 43.

Table 2. Calculated (th.) and experimental (exp.) bulk modulus (B_0) of the lattice parameters of $SnBi_2Te_4$ and $SnSb_2Te_4$ and their associated axial compressibilities.

	B_{0a} (GPa)	B_{0c} (GPa)	κ_a (10^{-3} GPa^{-1})	κ_c (10^{-3} GPa^{-1})
		$SnSb_2Te_4$		
exp.[a)]	42.4(2)	23.8(4)	7.9(3)	14(2)
th.(GGA-PBESol)[b)]	48(2)	30(4)	6.9(7)	11.1(15)
		α-Sb_2Te_3		
exp.[c)]	47.3(12)	22(3)	7.0(2)	15.0(5)
th.(GGA-PBESol)[b)]	48(1)	21(2)	6.94(14)	15.9(7)
		$SnBi_2Te_4$		
exp.[d)]	42.3(17)	25.3(17)	7.9(3)	13.1(9)
th.(GGA-PBESol)[d)]	48.0(15)	30(2)	6.9(7)	11.1(7)

[a)] This work; [b)] Calculations including SOC in this work; [c)] Calculated from data of Refs. 43 and 44; [d)] Data from Ref. 39, where calculations include SOC.

Table 3. Theoretical and experimental Raman-active mode frequencies and their pressure coefficients of $SnSb_2Te_4$ at room temperature as fitted with equation $\omega(P) = \omega_0 + aP + bP^2$ compared with those of theoretically simulated α-Sb_2Te_3.

	$SnSb_2Te_4$						**α-Sb_2Te_3**		
	Experiment			Theoretical Calculations[a)]			Theoretical Calculations[a)]		
Mode symmetry	ω_0 (cm^{-1})	a (cm^{-1} /GPa)	b (cm^{-1} /GPa^2)	ω_0 (cm^{-1})	a (cm^{-1} /GPa)	b (cm^{-1} /GPa^2)	ω_0 (cm^{-1})	a (cm^{-1} /GPa)	b (cm^{-1} /GPa^2)
E_g^1	-	-	-	38.87(15)	2.52(8)	-0.081(9)	50.4	2.62	-0.09
A_{2g}^1	53.3(8)	4.2(6)	-0.15(8)	55.3(2)	4.25(12)	-0.145(12)	68.9	4.3	-0.07
E_g^2	103.3(4)	3.7(7)	-0.4(2)	100.51(8)	2.45(6)	-	116.6	2.11	
A_{2g}^2	107.8(14)	4.6(6)	-0.15(6)	115.1(2)	2.70(18)	-	167.6	2.57	
E_g^3	-	-	-	116.65(17)	4.63(13)	-			
A_{2g}^3	160.87(14)	2.68(11)	-0.035(15)	167.10(16)	3.38(8)	-0.041(9)			

[a)] This work

Title ((no stars))

ToC figure ((Please choose one size: 55 mm broad × 50 mm high **or** 110 mm broad × 20 mm high. Please do not use any other dimensions))

((Supporting Information can be included here using this template))

Supporting Information

Supplementary Information of "Characterization and decomposition of the natural van der Waals $SnSb_2Te_4$ under compression"

Juan Ángel Sans, Rosario Vilaplana, Estelina Lora Da Silva, Catalin Popescu, Vanesa Paula Cuenca-Gotor, Adrián Andrada-Chacón, Javier Sánchez-Benitez, Oscar Gomis, André Luis de Jesus Pereira, Plácida Rodríguez-Hernández, Alfonso Muñoz, Dominik Daisenberger, Braulio García-Domene, Alfredo Segura, Daniel Errandonea, Ravhi Kumar, Oliver Oeckler, Philipp Urban, Julia Contreras-García, and Francisco J. Manjón*

Structural features of $SnSb_2Te_4$

In $SnSb_2Te_4$, roughly 50% of Sb cations are mixed with Sn cations in the 3a Wyckoff site and 25% of Sn are mixed with Sb cations in 6c atomic position. This result will not affect to the interlayer character featured by van der Waals interactions between Te sublayers. The similar covalent radii of Sn and Sb (1.39 Å in both)[S1] and ionic radii in an octahedral distribution, with a value of 83 Å for Sn and 90 Å for Sb[S2] suggests that the perturbation in the Sb-Te and Sn-Te octahedral units will be mostly influence by the electronic interactions, instead of geometrical effects. On the other hand, the isostructural $SnBi_2Te_4$ shows a similar mixed cationic occupancy as its counterpart $SnSb_2Te_4$. According to Kuropatawa and Kleinke,[S3] Sn remains mostly on the 3a atomic position with an occupancy of 74% like Bi that is in 6c atomic position with an occupancy of 68%.

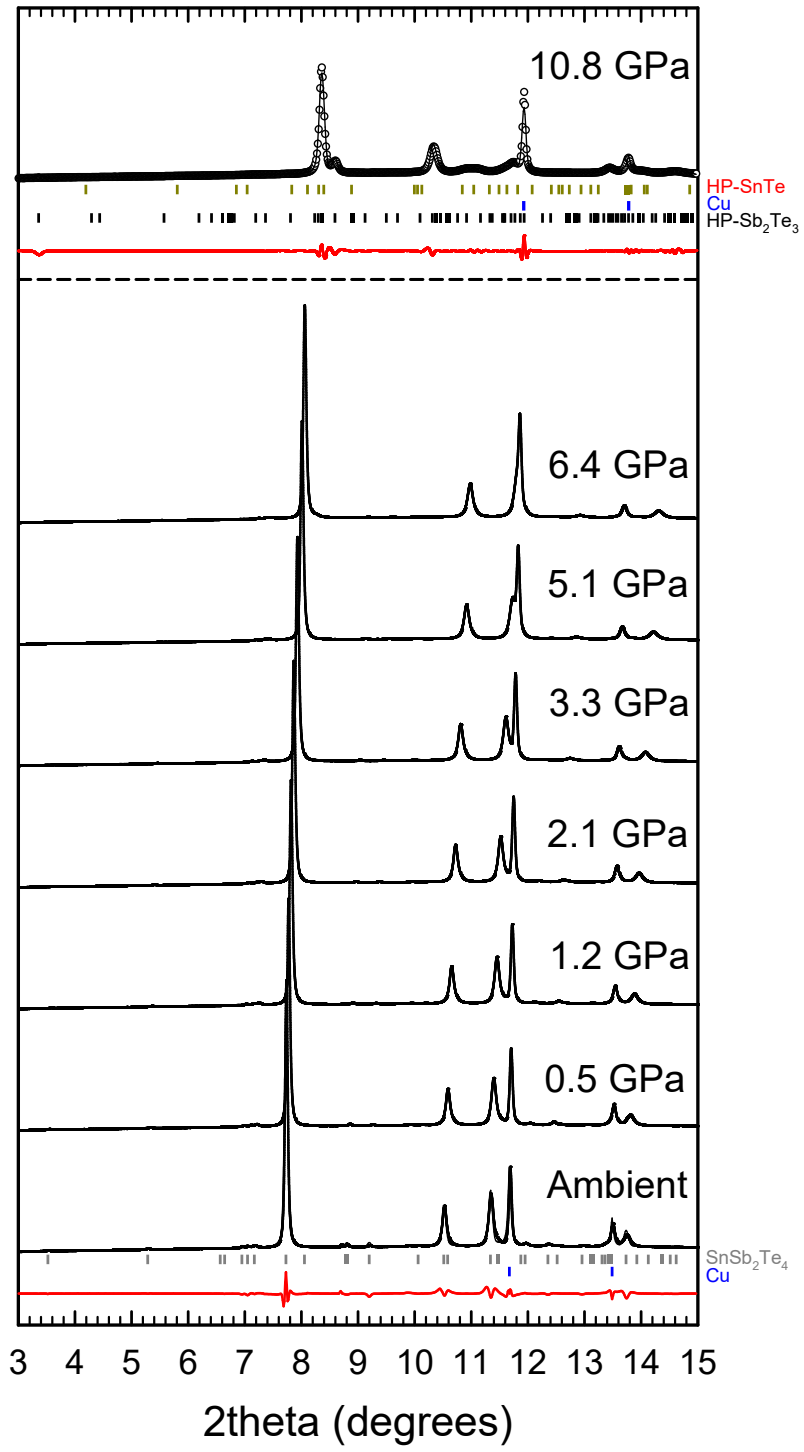

Figure S1. HP-ADXRD patterns of $SnSb_2Te_4$ at room temperature up to 11 GPa.

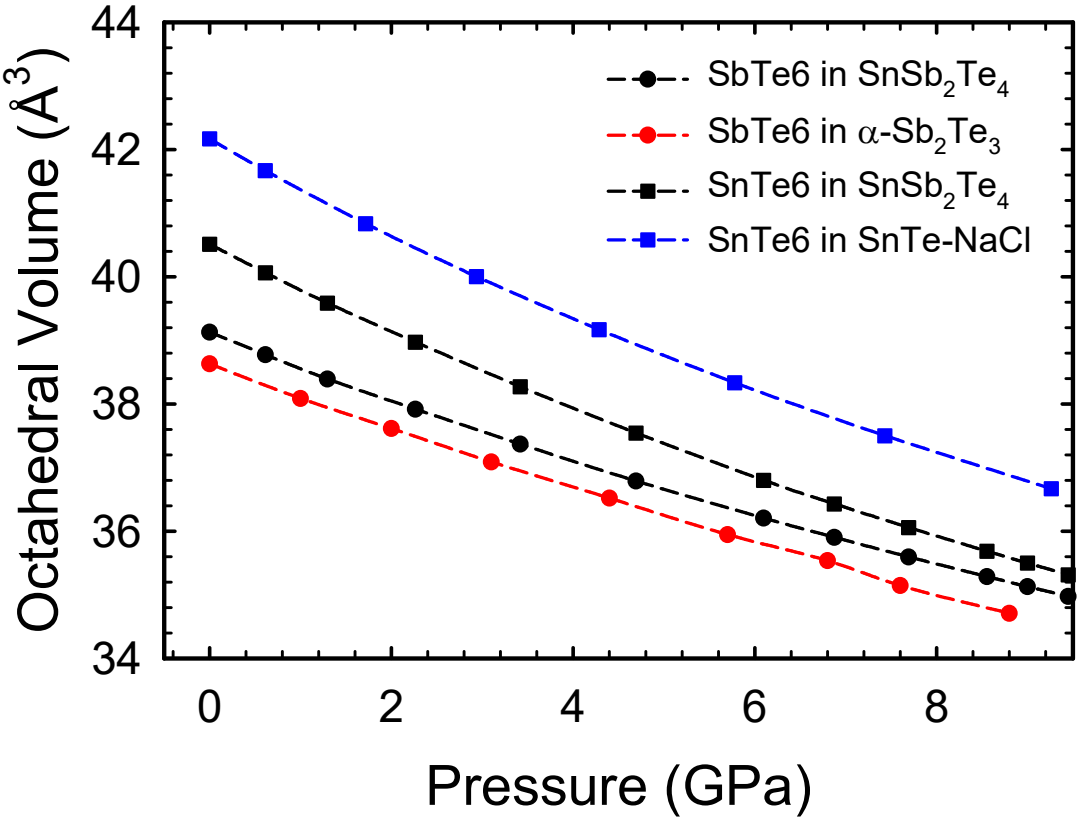

Figure S2. Pressure dependence of the theoretical volumes of $SbTe_6$ and $SnTe_6$ octahedra in $SnSb_2Te_4$ and in α-Sb_2Te_3[S6] and cubic SnTe.[S8]

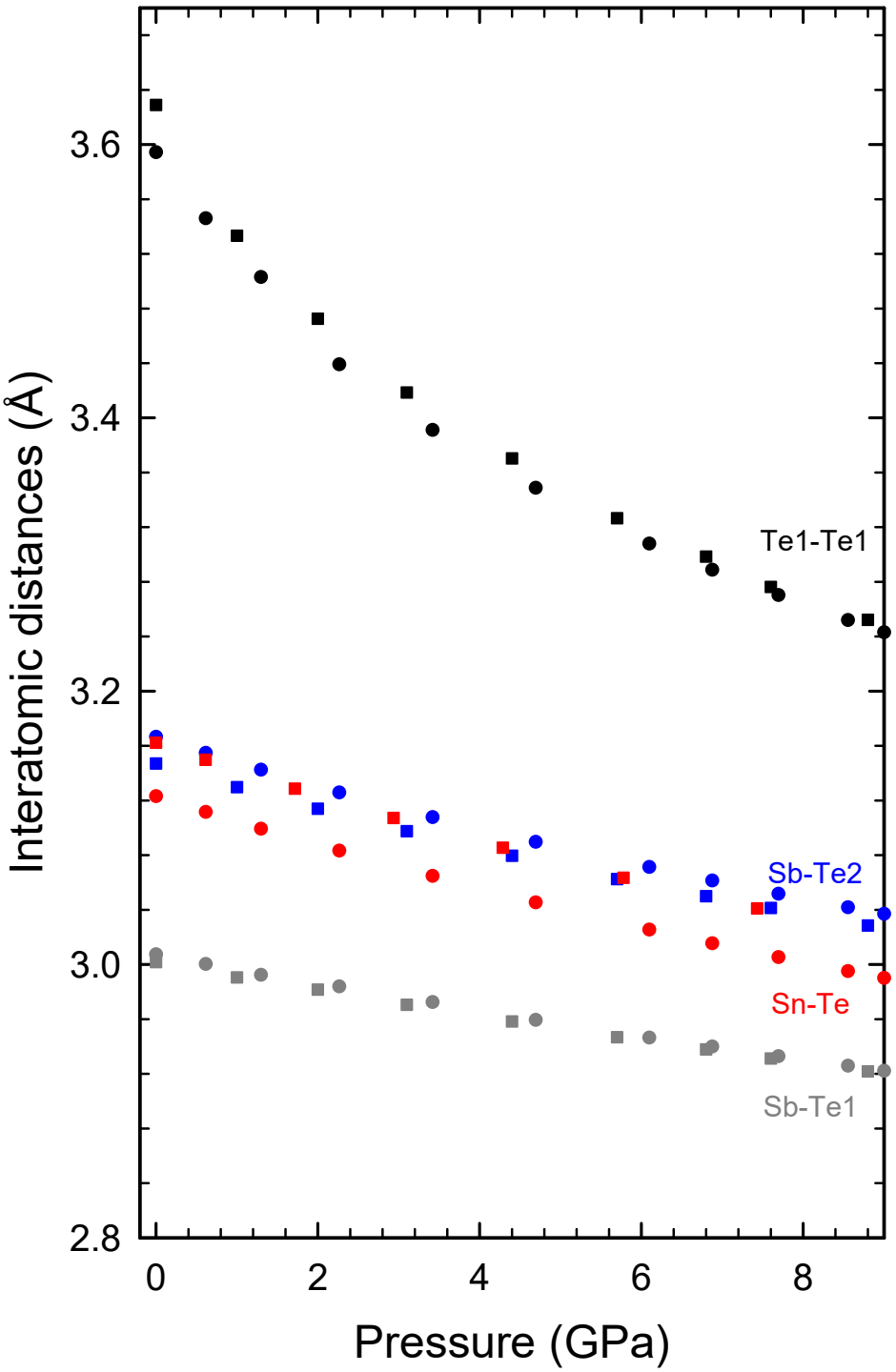

Figure S3. Pressure dependence of the theoretical interatomic distances in $SnSb_2Te_4$ (circles) and its binary constituents (squares), α-Sb_2Te_3 (blue, grey and black) and c-SnTe (red).

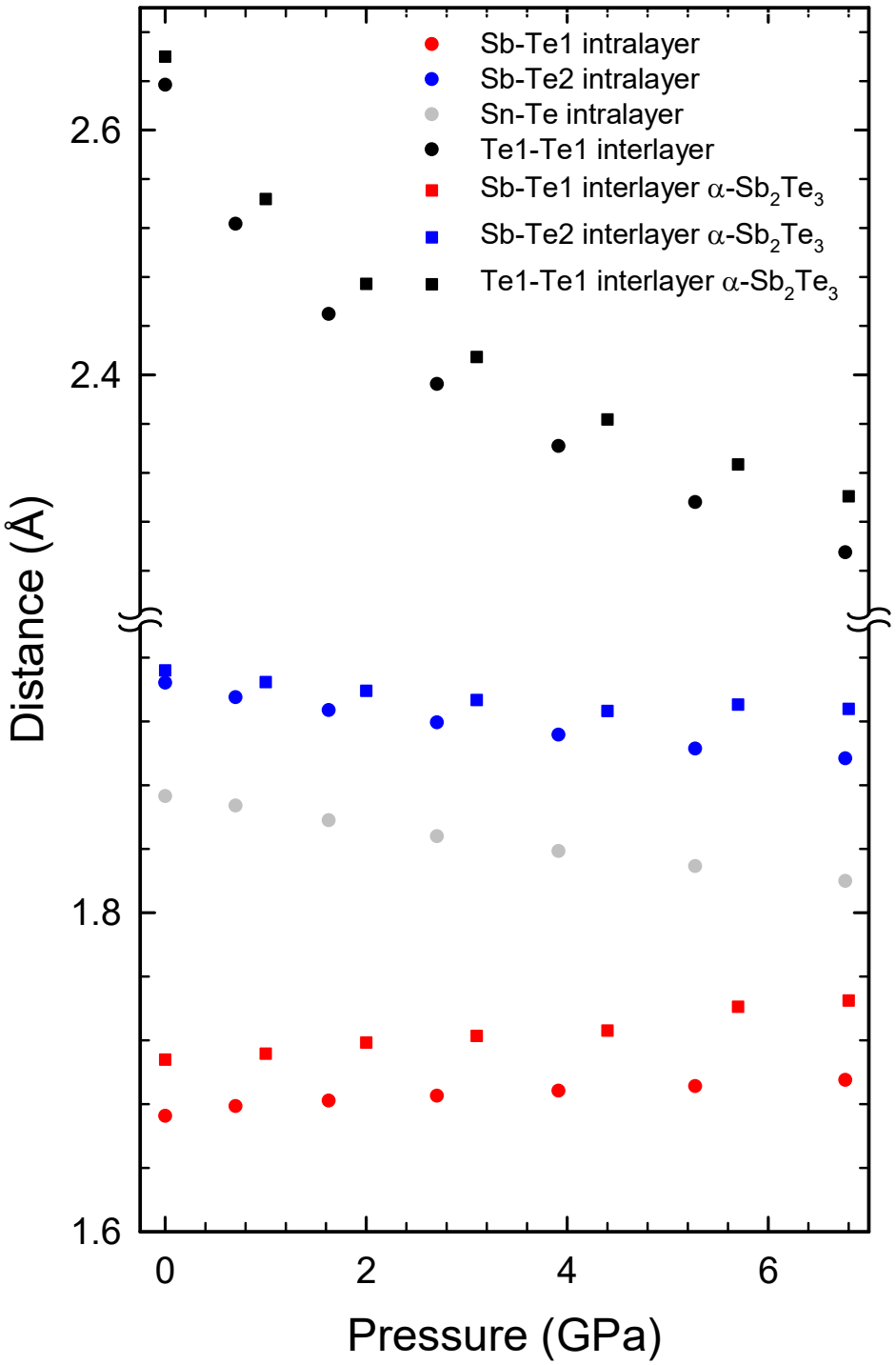

Figure S4. Pressure dependence of the theoretical interplanar distances: Te1-Te1 interlayer distance and the different intralayer distances in $SnSb_2Te_4$ (circles), and in α-Sb_2Te_3 and c-SnTe (squares).

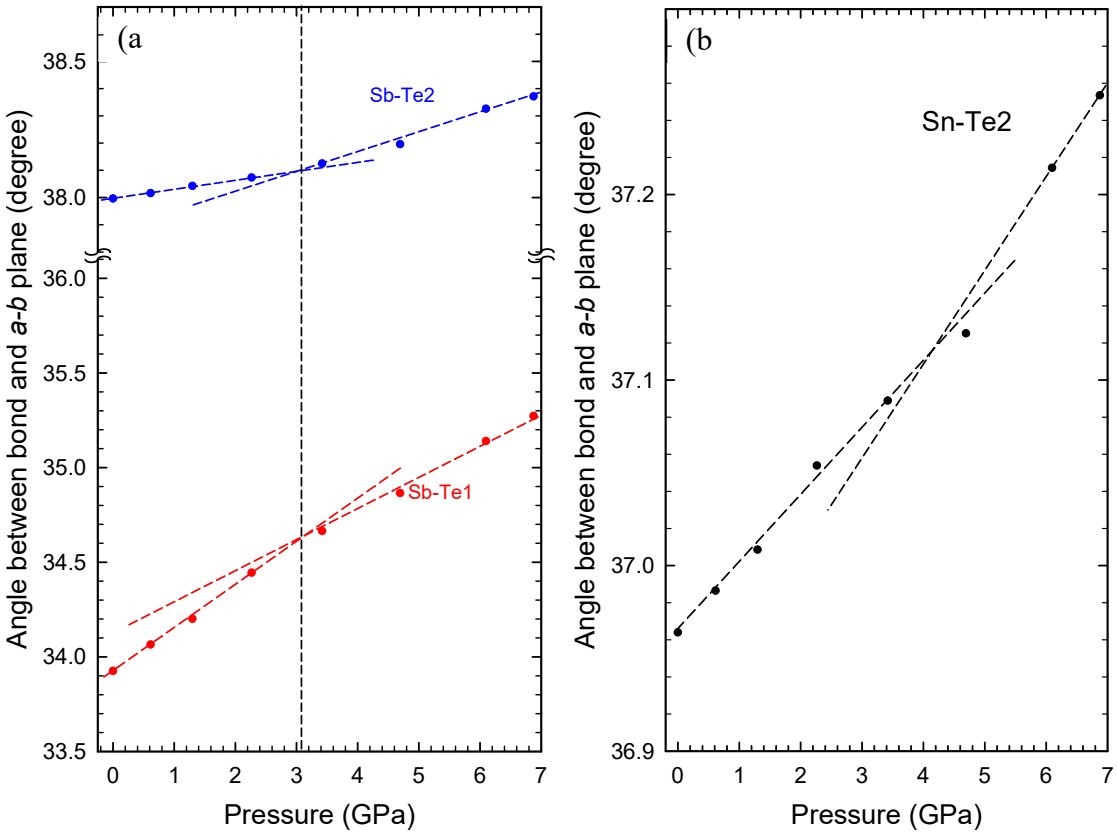

Figure S5. Pressure dependence of the theoretical angle between the *ab*-plane and the Sb-Te1 and Sb-Te2 (a) and Sn-Te (b) bonds in $SnSb_2Te_4$.

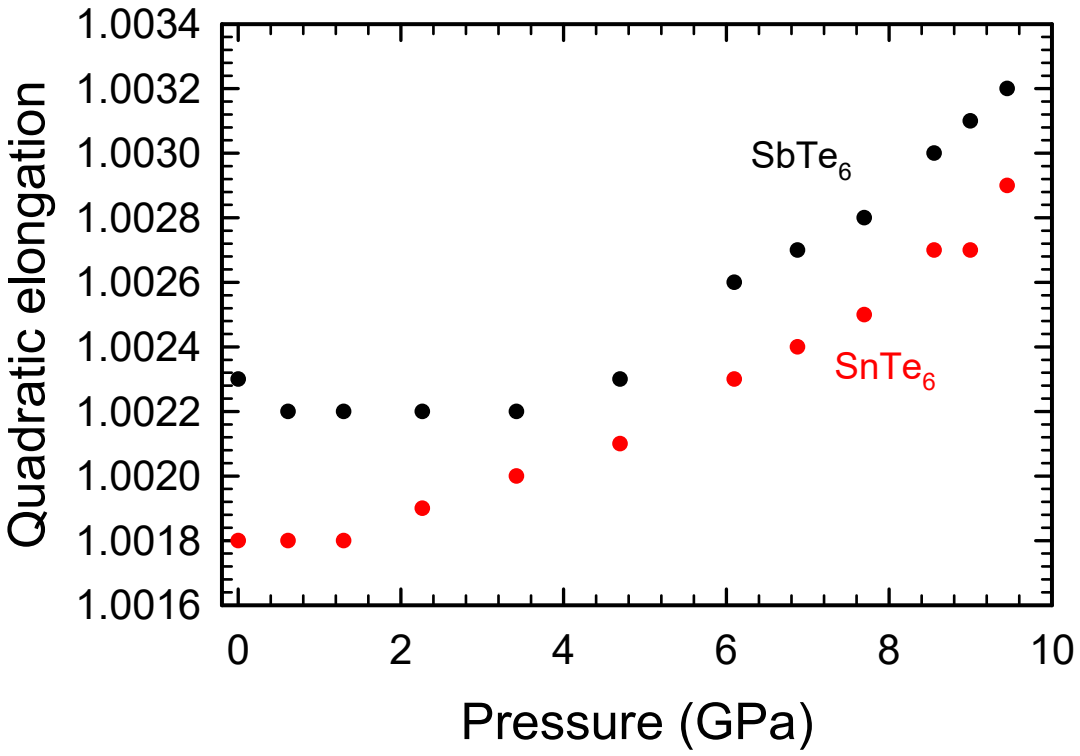

Figure S6. Pressure dependence of the theoretical quadratic elongation in the $SbTe_6$ and $SnTe_6$ octahedral units of $SnSb_2Te_4$.

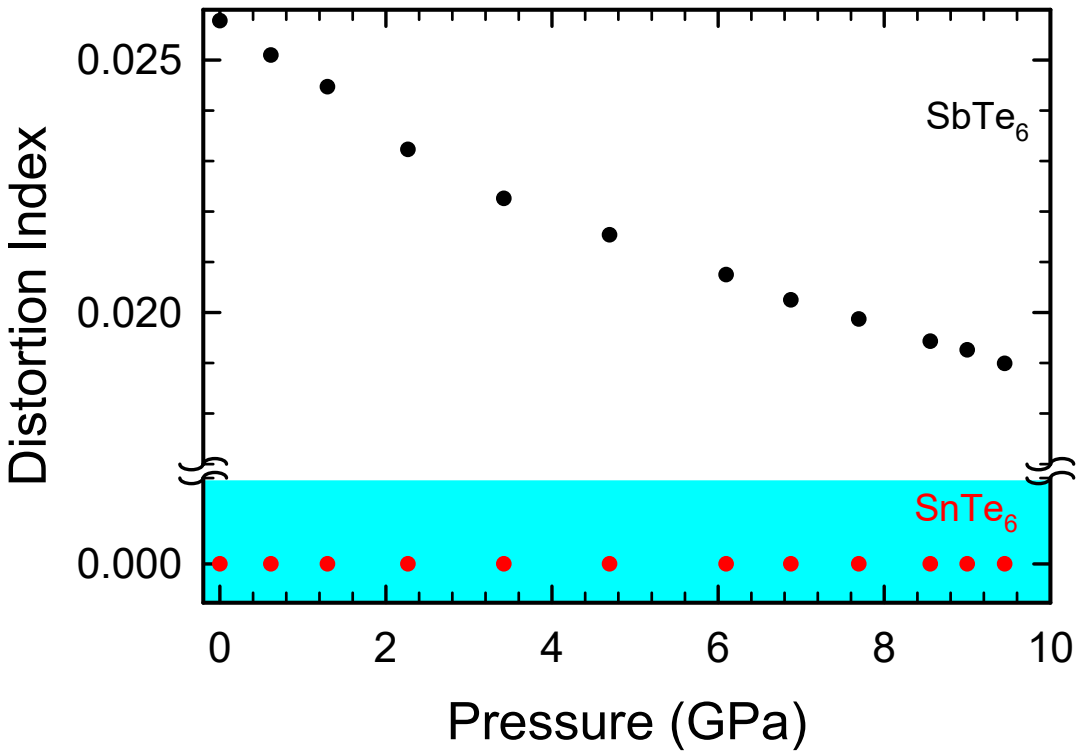

Figure S7. Pressure dependence of the theoretical distortion index of the $SbTe_6$ and $SnTe_6$ octahedral units of $SnSb_2Te_4$.

Vibrational modes in $SnSb_2Te_4$ at the Γ point

It is well-known that in layered materials, which usually crystallize either in rhombohedral, hexagonal or tetragonal space groups, the lowest-frequency E (doubly degenerated) and A (or B) modes at the point can be classified as interlayer modes (low-frequency phonons mainly characterized by out-of-phase vibrations of atoms corresponding to adjacent layers) or intralayer modes (medium- and high-frequency phonons mainly characterized by out-of-phase vibrations of atoms inside the layers). Interlayer E and A (or B) modes are grouped by pairs and are usually related to shear or transversal vibrations between adjacent layers along the layer plane (*a*-*b*) and to longitudinal vibrations of one layer against the adjacent ones (along the *c* axis), respectively. These are also known as rigid layer modes and both E and A (or B) interlayer modes arises from transversal acoustic (TA) and longitudinal acoustic (LA) modes, respectively, due to the folding of the Brillouin-zone (BZ) border into the **Γ**-point due to the decreasing symmetry from cubic to hexagonal or tetragonal. Similarly, E and A (or B) intralayer modes come from transversal optic (TO) and longitudinal optic (LO) modes at **Γ** and from additional modes due to the folding of the BZ border into the **Γ** point.

The number of interlayer and intralayer modes in layered materials depends on the complexity of the unit cell. In the simplest case, there should be two interlayer modes (one of E symmetry and one A or B symmetry) and two intralayer modes, such as what occurs SnS_2 **[S4]**. In the case of $SnSb_2Te_4$, there are two almost pure interlayer modes (E_g^1 and A_{1g}^1), which have the lowest frequencies and are Raman-active and correspond to out-of-phase movements of the neighbor layers both along the *a*-*b* plane (E_g^1 mode) and along *c* axis (A_{1g}^1 mode). Similar to other Raman-active modes, these modes are characterized by the immobility of the central Sn atom located in a highly symmetric Wyckoff site, the in-phase movements of all atoms of each sublayer above and below the central Sn plane and the out-of-phase movement of the

atoms in the two sublayers (see **Figure S8**). Furthermore, it can be observed that both the frequency and pressure coefficients of the interlayer A mode is larger than that of the interlayer E mode as what typically occurs in van der Waals-type layered compounds (see **Tables S1 and S2 and Figs. 6 and S19**).

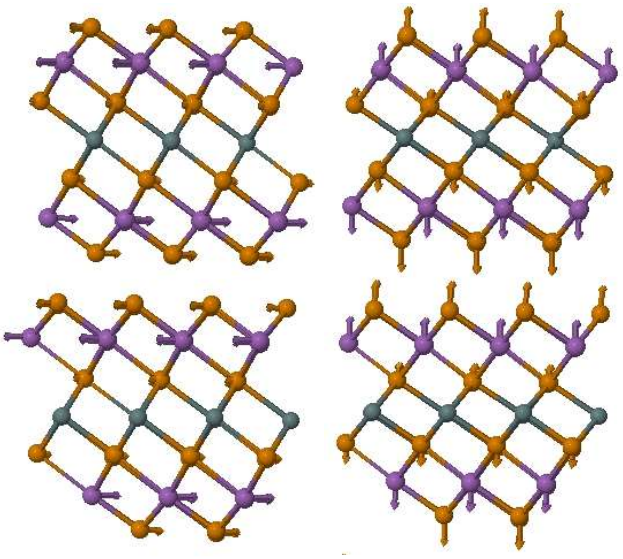

Figure S8. Atomic movements (see arrows) of low-frequency interlayer Raman-active modes E_g^1 (left) and A_{1g}^1 (right) located near 38 and 55 cm^{-1} at room pressure, respectively. Sn, Sb and Te atoms are depicted in green, purple and orange colors, respectively.

The next couple of E and A modes, discussed in order of increasing frequency, is formed by the low-frequency E_u^1 mode and the A_{2u}^1 mode (see **Figure S9**). These two intralayer modes are characterized by an out-of-phase vibration of the central Sn atoms and the external Sb atoms. The E_u^1 mode is characterized by a vibration of the central $SnTe_6$ unit against the external $SbTe_3$ units in the a-b plane. The A_u^1 mode is the complementary mode to the E_u^1 mode and it is characterized by an out-of-phase vibration of the central $SnTe_6$ unit against the external $SbTe_3$ units along the *c*-axis.

We may observe that while all A_{2u} and E_u modes show an in-phase vibration of the neighbor Te atoms on adjacent layers, all A_{1g} and E_g modes evidence out-of-phase vibrations of

neighbor Te atoms on adjacent layers similar to those modes of the pure interlayer modes. Note, however, that the intralayer modes are clearly dominated by the strong vibration amplitudes of intralayer structures. Similarly, it can be observed that the vibration of the central Sn atom is observed in all ungerade (IR-active) modes, whereas the Sn atom is mainly static in characterized by the gerade (Raman-active) modes.

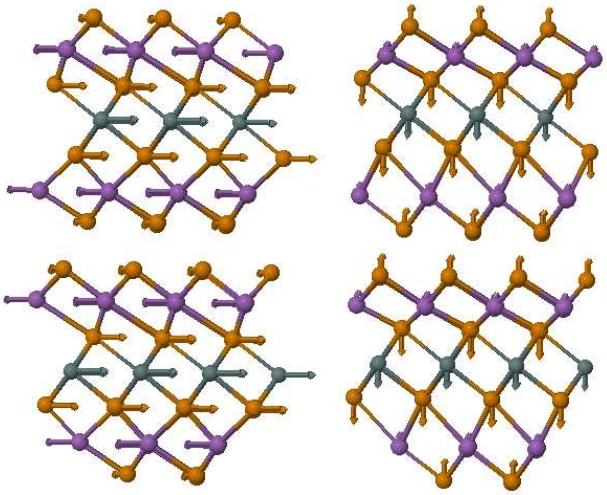

Figure S9. Atomic movements of IR-active modes E_u^1 (left) and A_{2u}^1 (right) located near 62 and 81 cm^{-1} at room pressure, respectively. Sn, Sb and Te atoms are depicted in green, purple and orange colors, respectively.

The following couple of E and A modes, in order of increasing frequency, is formed by the low-frequency E_u^2 mode and the middle-frequency A_{2u}^2 mode (see **Figure S10**). These two intralayer modes are characterized by an in-phase vibration of the central Sn atoms and the external Sb atoms against the Te atoms. The E_u^2 mode is characterized by the vibration of the network of Sn and Sb atoms against the network of Te atoms along the a-b plane; i.e., it is the main asymmetric bending mode of the Sn-Te bond in the central $SnTe_6$ unit. On the other hand, the A_{2u}^2 mode is the complementary mode to the E_u^2 mode and it is characterized by an in-phase vibration of the central Sn atom and the Sb atoms against the network of Te atoms along the *c*-axis; i.e., it is the main asymmetric stretching mode of the Sn-Te bond in the

central $SnTe_6$ unit. Therefore, these two modes are characteristic of the $SnTe_6$ octahedron and do not occur in Sb_2Te_3 as we will comment later.

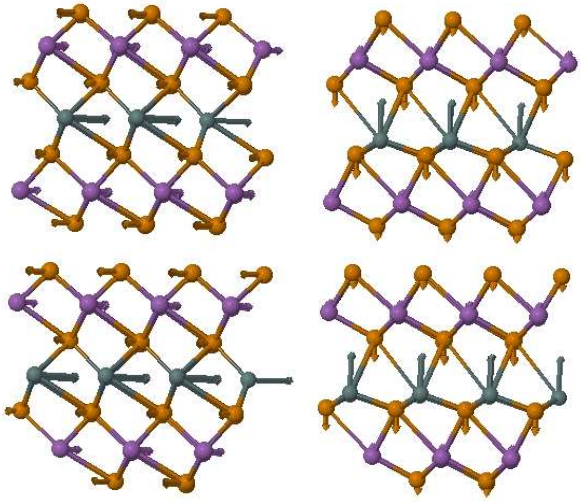

Figure S10. Atomic movements of IR-active mode E_u^2 (left) and A_{2u}^2 (right) located near 65 and 104 cm^{-1} at room pressure, respectively. Sn, Sb and Te atoms are depicted in green, purple and orange colors, respectively.

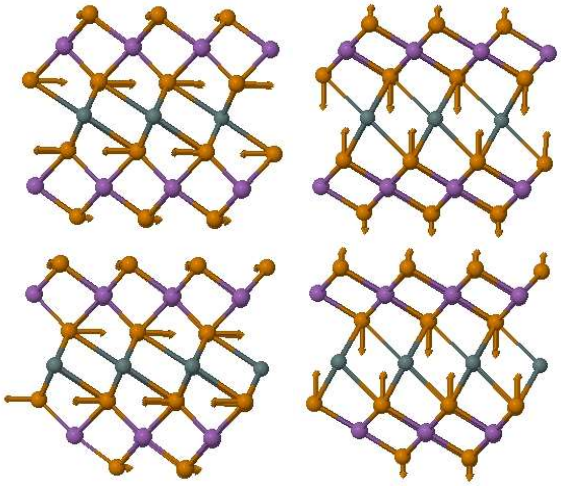

Figure S11. Atomic movements of middle-frequency Raman-active modes E_g^2 (left) and A_{1g}^2 (right) located near 100 and 115 cm^{-1} at room pressure, respectively. Sn, Sb and Te atoms are depicted in green, purple and orange colors, respectively.

The next two modes, discussed in order of increasing frequency, is formed by the medium-frequency E_g^2 and A_{1g}^2 modes (see **Figure S11**). The E_g^2 mode is characterized by the strong out-of-phase vibration of the Te atoms close to the central Sn atoms along the *a-b* plane; i.e., it is the main symmetric bending mode of the Sn-Te of the central $SnTe_6$ unit. The A_{1g}^2 mode is the complementary mode to the E_g^2 and it is characterized by the strong vibration of Te atoms against Sn and Sb atoms alternately along the *c* axis; i.e., it is the main symmetric stretching mode of the Sn-Te bond in the central $SnTe_6$ unit. Again, these two modes are characteristic of the $SnTe_6$ octahedron and do not occur in α-Sb_2Te_3 as we will comment further on.

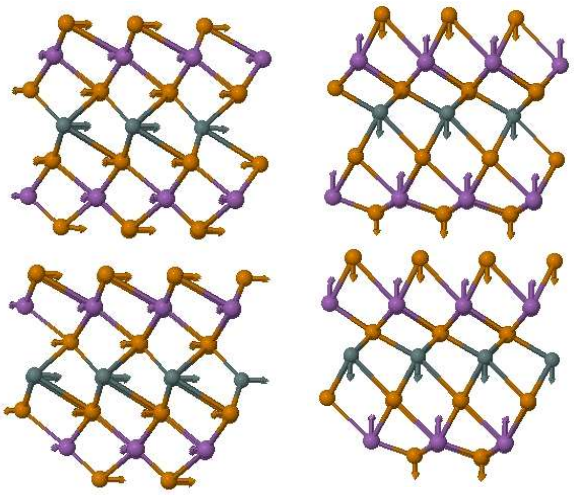

Figure S12. Atomic movements of IR-active modes E_u^3 (left) and A_u^3 (right) located near 112 and 157 cm^{-1} at room pressure, respectively. Sn, Sb and Te atoms are depicted in green, purple and orange colors, respectively.

The next pair of frequencies are formed by the medium-frequency E_u^3 mode and the high-frequency A_u^3 mode (see **Figure S12**). These two intralayer modes are characterized by an out-of-phase vibration of the central Sn atoms and the external Sb atoms as in the E_u^1 and A_u^1 modes. Regarding the E_u^1 mode, the central Te atoms show an in-phase vibration with the central Sn atom leading to a vibration of the central $SnTe_6$ unit against the external $SbTe_3$ units in the a-b plane; however, for the E_u^3 mode the central Sn atom shows an out-of-phase

vibration with respect to the adjacent Te atoms as what occurs for a Sn-Te bending mode of the $SnTe_6$ unit. Additionally, since the external Te atoms vibrate out-of-phase with respect to the Sb atoms, such a vibrational mode results also in a symmetric Sb-Te bending mode of the $SbTe_6$ unit. Similarly, the A_u^1 mode is an out-of-phase vibration of the central $SnTe_6$ unit against the external $SbTe_3$ units along the c axis; however, the A_u^3 mode corresponds solely to the central Sn atom that vibrates against the external Sb atoms in an asymmetric way (central Te atoms are static), thus leading to a coupled asymmetric Sn-Te and Sb-Te stretching mode of both $SnTe_6$ and $SbTe_6$ units.

Finally, the last two intralayer modes, referenced in order of increasing frequency is formed by the medium-frequency E_g^3 mode and the high-frequency A_g^3 mode (see **Figure S13**). Both the E_g^3 and A_g^3 modes are characterized by the small vibration of the central $SnTe_6$ unit, such as what occurs for the E_g^1 and A_g^1 modes; however, for the E_g^1 and A_g^1 modes, the Sb atoms vibrate in phase with adjacent Te atoms, whereas in the E_g^3 and A_g^3 modes, external Te and Sb atoms move out-of-phase. Additionally, for both four modes there is an out-of-phase movement of all atoms in the two sublayers. In this way, atomic movements of Te and Sb atoms along the a-b plane evidence the E_g^3 mode as being the asymmetric bending mode of Sb-Te in the $SbTe_6$ units. Alternatively, the complementary A_g^3 mode shows Te and Sb atoms moving out-of-phase along the c axis, therefore this mode can be viewed as the asymmetric stretching mode of Sb-Te of the $SbTe_6$ units.

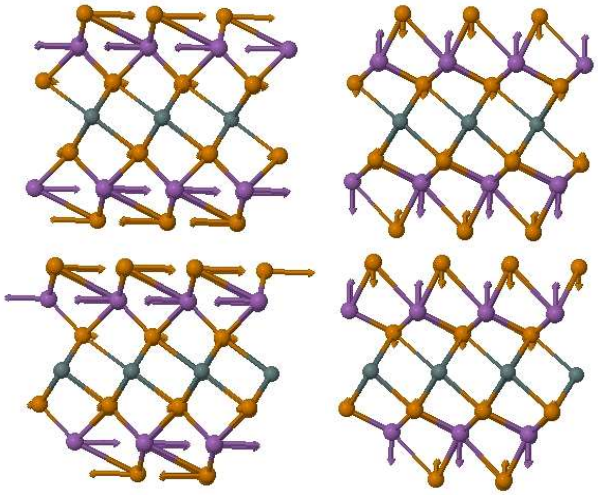

Figure S13. Atomic movements of Raman-active modes E_g^3 and A_g^3 located near 117 and 167 cm^{-1} at room pressure, respectively. Sn, Sb and Te atoms are depicted in green, purple and orange colors, respectively.

A first comparison can be stablished between the vibrational modes at Γ in $SnSb_2Te_4$ and the parent compound Sb_2Te_3. In Sb_2Te_3 there are four Raman-active modes (E_g^1, A_{1g}^1, E_g^2 and A_{1g}^2) and four IR-active modes (E_u^1, E_u^2, A_{2u}^1 and A_{2u}^2) and referenced in order of increasing frequency **[S5,S6]**. As regards to the Raman-active modes, the interlayer modes of α-Sb_2Te_3 are the E_g^1 and A_{1g}^1 modes (**Figure S14**) and these are similar to the E_g^1 and A_g^1 modes of $SnSb_2Te_4$ (**Figure S8**). For all these modes the central part of the layer remains almost static and the external adjacent Sb and Te atoms in a sublayer vibrate in-phase and also out-of-phase with respect to the atoms of the other adjacent sublayer. Similarly, the intralayer E_g^2 and A_{1g}^2 modes of Sb_2Te_3 (**Figure S15**) are similar to the intralayer E_g^3 and A_g^3 modes of $SnSb_2Te_4$ (**Figure S13**) since for all these modes the central part of the layer remains almost static and the external adjacent Sb and Te atoms in a sublayer vibrate, among them and with respect to atoms of the other sublayer, out-of-phase. The similarity of E_g^2 and A_{1g}^2 modes in Sb_2Te_3 and E_g^3 and A_g^3 modes in $SnSb_2Te_4$ is so remarkable that these modes possess practically the same theoretically predicted frequency values (see **Table S1**). With respect to the Raman-active E_g^2 and A_g^2 modes of $SnSb_2Te_4$ (**Figure S11**), these have no analog on α-Sb_2Te_3 since both

modes involve out-of-phase vibrations of the internal Te atoms, which cannot occur in Sb_2Te_3 with only one internal Te atom.

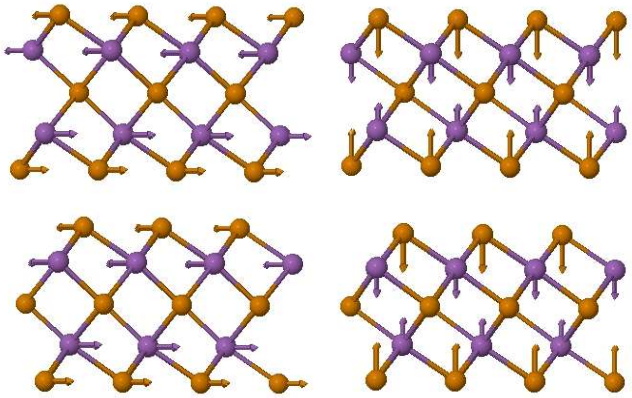

Figure S14. Atomic movements (see arrows) of low-frequency interlayer Raman-active modes E_g^1 and A_{1g}^1 in Sb_2Te_3 located near 50.4 and 68.9 cm^{-1} at room pressure, respectively. Sb and Te atoms are depicted in purple and orange colors, respectively.

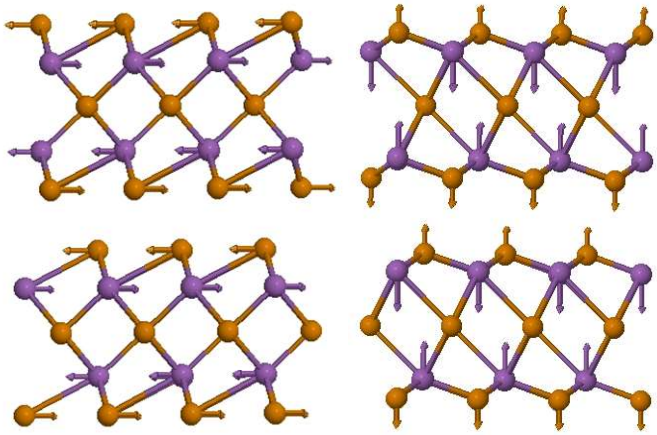

Figure S15. Atomic movements (see arrows) of high-frequency intralayer Raman-active modes E_g^2 and A_{1g}^2 in Sb_2Te_3 located near 116.6 and 167.6 cm^{-1} at room pressure, respectively. Sb and Te atoms are depicted in purple and orange colors, respectively.

With respect to the IR-active modes, the E_u^1 ($E_u(2)$ in **[S5]**) and A_{2u}^2 ($A_{2u}(3)$ in **[S5]**) modes of Sb_2Te_3 are similar to the E_u^2 and A_u^2 modes of $SnSb_2Te_4$. For both modes of Sb_2Te_3, Sb atoms vibrate in-phase in the two sublayers and vibrate out-of-phase with respect to all Te atoms as what occurs for the E_u^2 and A_u^2 modes of $SnSb_2Te_4$. Note that the movement of the central Te atoms of the A_{2u}^2 mode is very low (not shown in **Figure S16**) but in phase with

the other Te atoms, similar to the A_u^2 mode of $SnSb_2Te_4$. On the other hand, the E_u^2 ($E_u(3)$ in **[S5]**) and A_{2u}^1 ($A_{2u}(2)$ in **[S5]**) modes of Sb_2Te_3 are similar to the E_u^3 and A_u^3 modes of $SnSb_2Te_4$. For both E_u^2 and A_{2u}^1 modes of Sb_2Te_3 central Te atoms vibrate out-of-phase with respect to the external Te atoms as to what is observed for the E_u^3 and A_u^3 modes of $SnSb_2Te_4$.

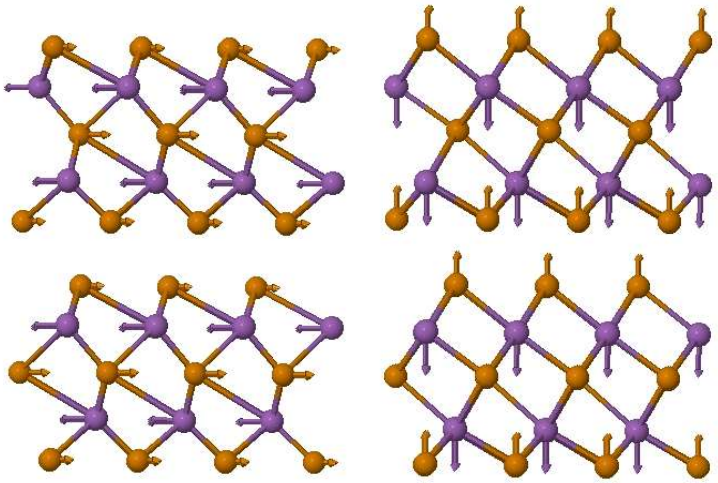

Figure S16. Atomic movements (see arrows) of intralayer IR-active modes E_u^1 and A_{2u}^2 in Sb_2Te_3 located near 78.0 and 138.7 cm^{-1} at room pressure, respectively. Sb and Te atoms are depicted in purple and orange colors, respectively.

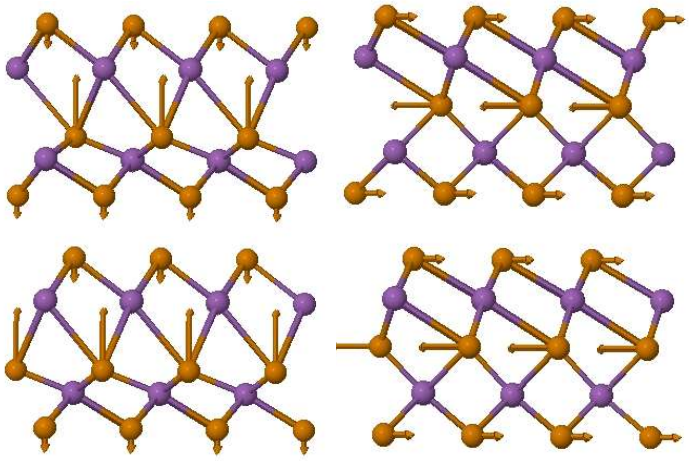

Figure S17. Atomic movements (see arrows) of intralayer IR-active modes E_u^2 and A_{2u}^1 in Sb_2Te_3 located near 100.4 and 109.9 cm^{-1} at room pressure, respectively. Sb and Te atoms are depicted in purple and orange colors, respectively.

Finally, it is noteworthy of mentioning that the IR-active E_u^1 and A_u^1 modes of $SnSb_2Te_4$ have no resemblance with IR-active modes in Sb_2Te_3. Note that these two modes refer to the Sb atoms vibrating in-phase with their adjacent external Te atoms, a feature that does not occur in any of the IR-active modes of Sb_2Te_3. Finally, it must be stressed that for all IR-active modes of α-Sb_2Te_3, Sb atoms of the two sublayers vibrate in-phase, while for all Raman-active modes of α-Sb_2Te_3 vibrate out-of-phase. The same behavior is observed in $SnSb_2Te_4$. This is the main characteristic to discern between Raman-active and IR-active modes of both compounds.

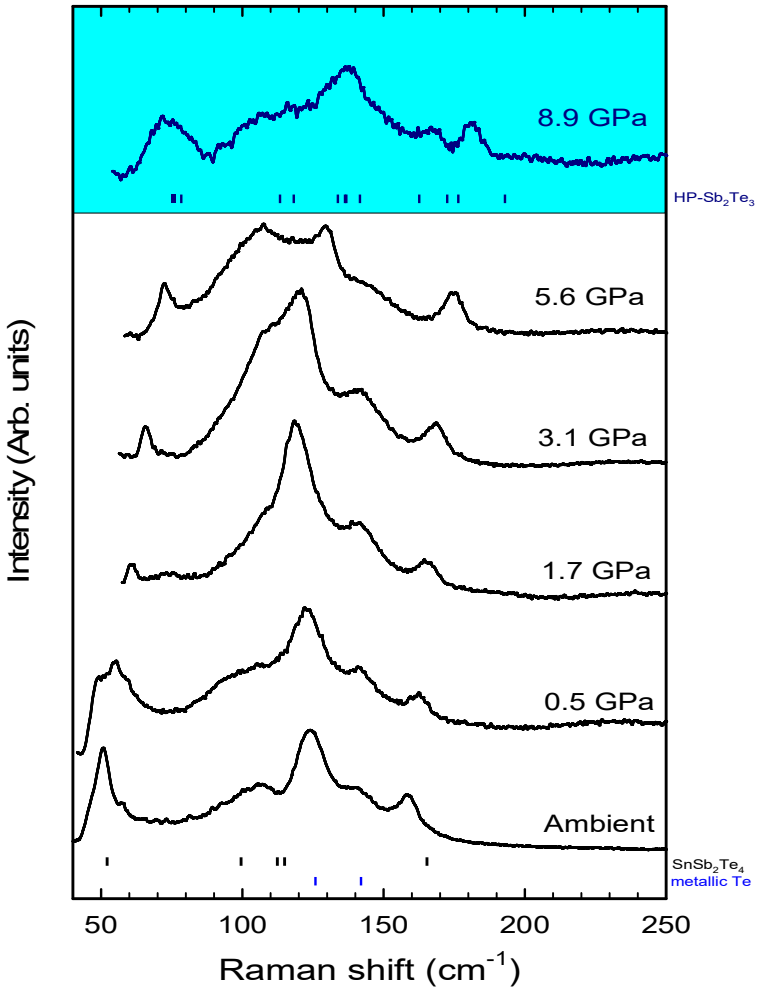

Figure S18. Raman scattering spectra of rhombohedral $SnSb_2Te_4$ at different pressures up to 8.9 GPa. Black (blue) vertical ticks correspond to theoretically predicted Raman-active mode frequency of $SnSb_2Te_4$ (Metallic Te).

Referring to the pressure coefficients of the different Raman-active and IR-active modes, it can be observed that generally the A modes have larger pressure coefficients than their associated E modes, as it is expected in non-polar layered compounds with van der Waals forces between their layers (see **Tables S1 and S2**). This has been already commented for interlayer Raman-active E_g^1 and A_{2g}^1 modes and it applies to both $SnSb_2Te_4$ and Sb_2Te_3. Usually, the small pressure coefficient of the low-frequency E mode in layered materials is ascribed to the weak bending force constant due to weak van der Waals forces between the

neighboring layers. On the other hand, the large pressure coefficient of the low-frequency A mode is due to the extraordinary increase of the stretching force constant between neighboring layers due to the strong decrease of the interlayer distance.[S4,S7] This behavior is also found for the low-frequency interlayer modes in layered Sb_2Te_3 and $SnSb_2Te_4$, and it is also valid for the other pairs of intralayer E and A modes, previously commented. This can be understood if intralayer E modes are mainly associated to bending Sb-Te (Sb-Te and Sn-Te) modes in Sb_2Te_3 ($SnSb_2Te_4$), while intralayer A modes are mainly associated to stretching Sb-Te (Sb-Te and Sn-Te) modes in Sb_2Te_3 ($SnSb_2Te_4$). This reasoning allows also to explain the reason for which the A modes always possess larger frequencies than their associated E modes.

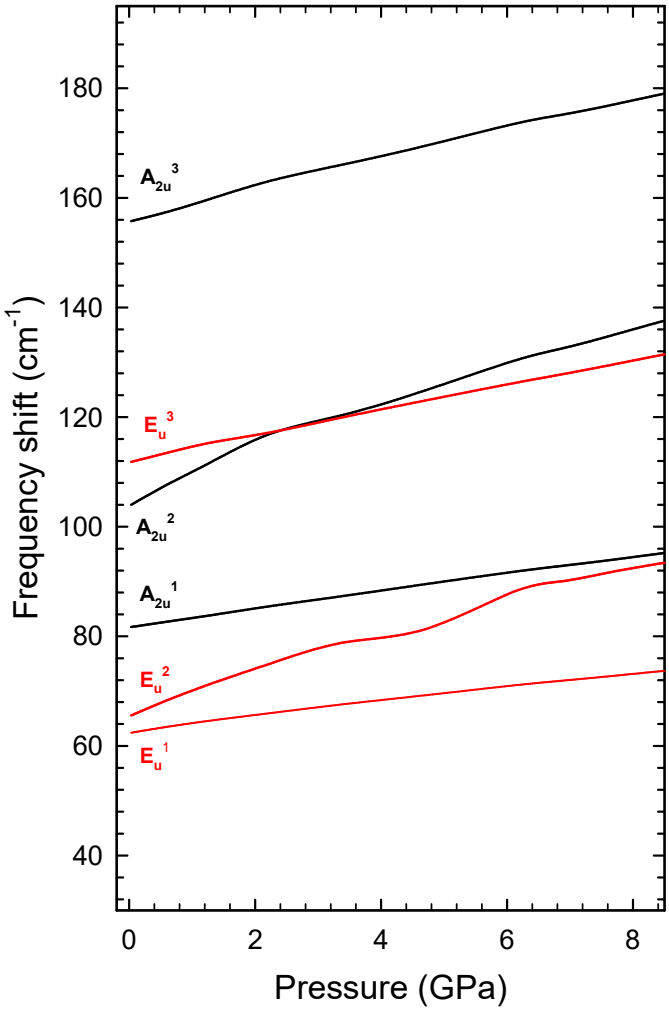

Figure S19. Pressure dependence of the theoretical IR-active modes of $SnSb_2Te_4$. A modes and doubly-degenerate E modes are depicted in black and red, respectively.

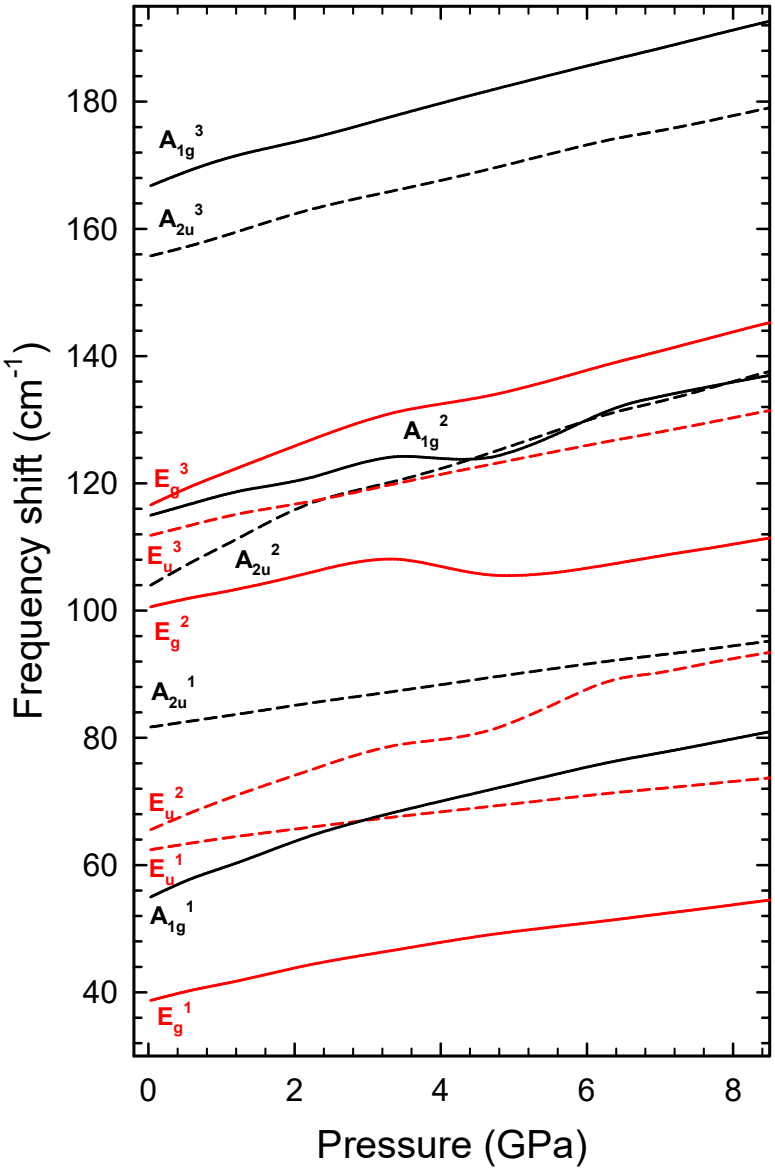

Figure S20. Pressure dependence of the theoretical (solid lines) Raman-active and (dashed lines) infrared-active mode frequencies of $SnSb_2Te_4$.

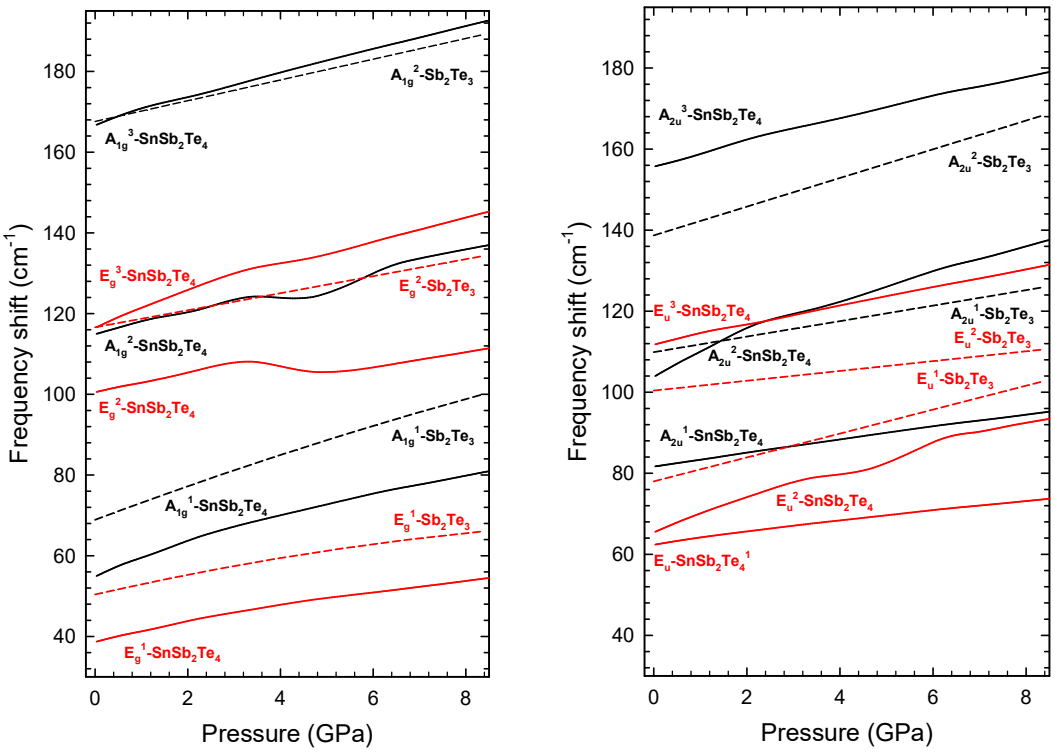

Figure S21. Pressure dependence of the theoretical (left) Raman-active and (right) infrared-active mode frequencies of $SnSb_2Te_4$ and Sb_2Te_3.

The most notable deviation of the rule mentioned above of the Raman-active modes, is that of the E_g^3 mode in $SnSb_2Te_4$. The theoretical pressure coefficient of this mode is larger than its associated A_{2g}^3 mode. This feature contrasts with Sb_2Te_3 where the equivalent modes E_g^2 and A_{2g}^2 show a normal behavior. Additionally, it must be noted that the pressure coefficient at zero pressure obtained for the A_{2g}^2 mode in $SnSb_2Te_4$ is quite high because the fit has been performed with high-pressure data due to the lack of values near room pressure.

The larger pressure coefficient of the A modes when compared to their corresponding E modes also applies for IR-active modes. Note that in Sb_2Te_3 the pressure coefficient of E_u^1 mode is smaller than its associated A_{2u}^2 mode and that of the E_u^2 mode is smaller than its associated A_{2u}^1 mode. This reasoning also applies to their similar IR-active modes in $SnSb_2Te_4$; i.e., the E_u^2 and A_{2u}^2 and the E_u^3 and A_{2u}^3 modes, respectively. Moreover, the same

rule applies to E_u^1 and A_{2u}^1 modes in $SnSb_2Te_4$ that have no correspondence in α-Sb_2Te_3. This similarity between Raman and IR modes both in Sb_2Te_3 and $SnSb_2Te_4$ remarks the strangely large pressure coefficient of the theoretical E_g^3 mode (which is almost double from its expected value) in $SnSb_2Te_4$, since the Raman-active A_{2g}^3 mode has a similar value of the pressure coefficient than its IR-active counterpart (the A_{2u}^3 mode).

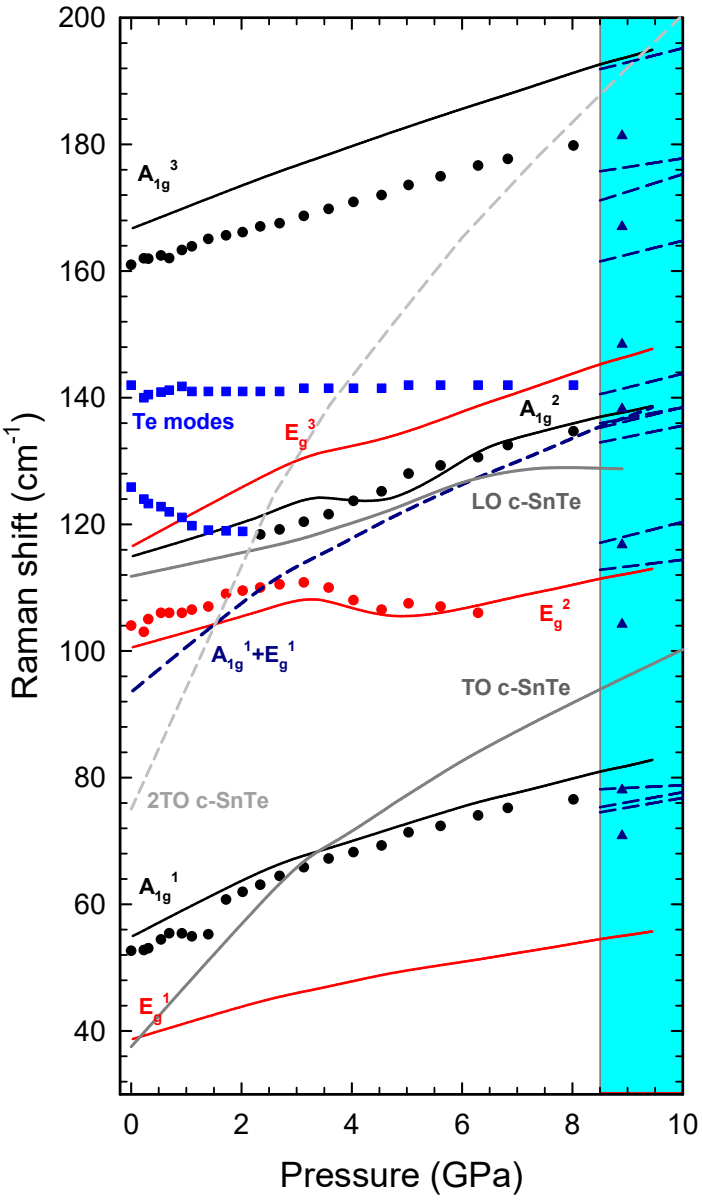

Figure S22. Pressure dependence of the experimental (symbols) and theoretical (lines) Raman-active mode frequencies in $SnSb_2Te_4$ together with the representation of theoretical LO and TO IR-active modes of c-SnTe. Dashed lines represent the pressure dependence of the $A_{1g}^1 + E_g^1$ combination at Γ in $SnSb_2Te_4$ and the 2TO mode at Γ in c-SnTe.

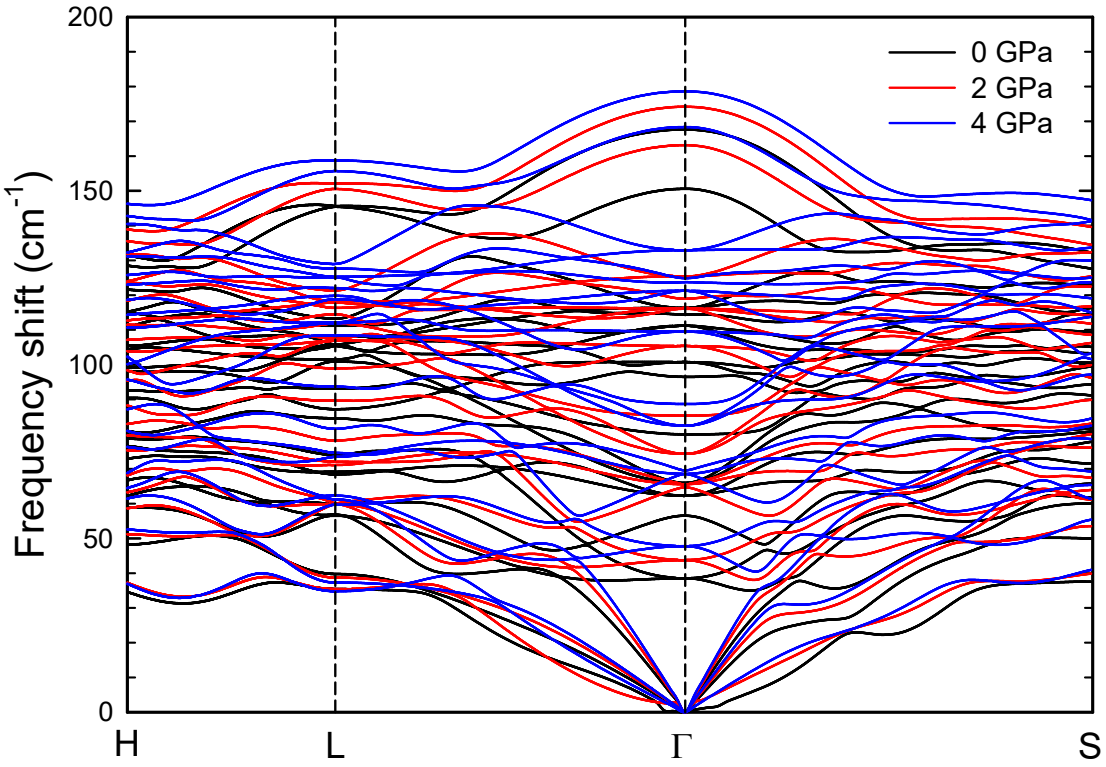

Figure S23. Phonon dispersion curves of $SnSb_2Te_4$ at 0, 2 and 4 GPa.

Evolution of the electronic topology under pressure

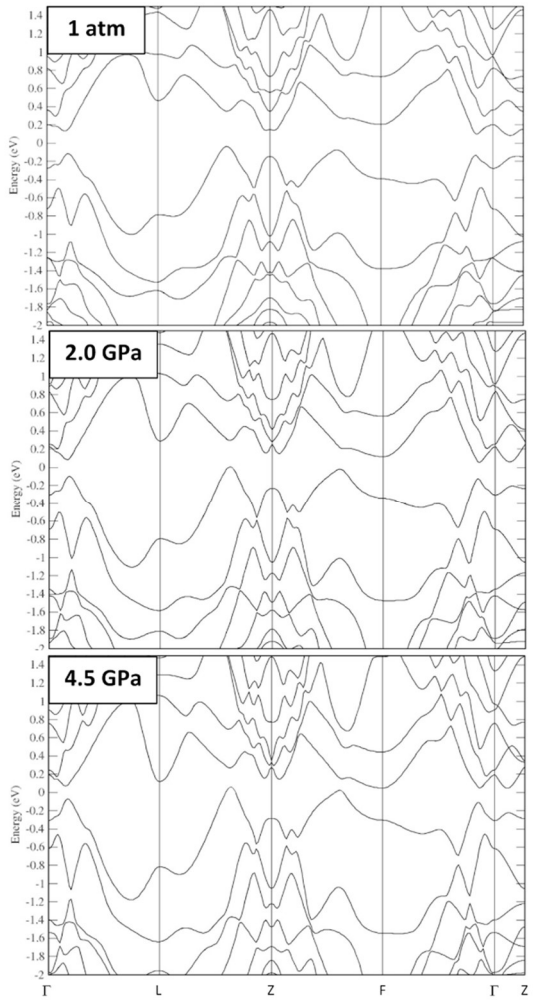

Figure S24. *Ab-initio* calculated band electronic structure of $SnSb_2Te_4$ theoretically predicted at 1 atm (top), 2 GPa (middle), and 4.5 GPa (bottom).

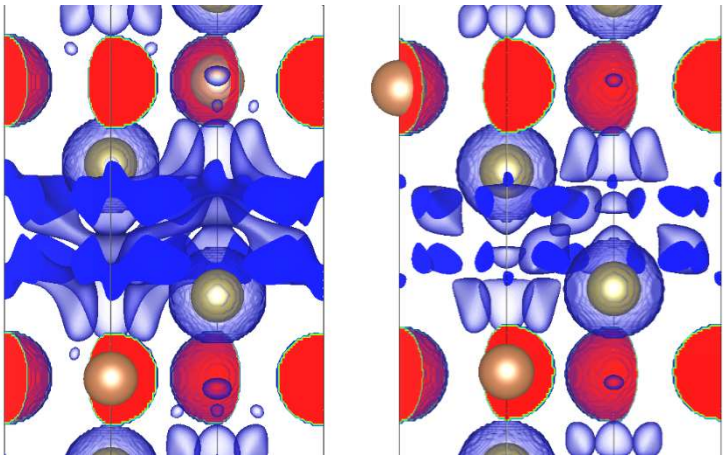

Figure S25. Reduced density gradient map of rhombohedral $SnSb_2Te_4$ around the interlayer space at 1 atm (left) and 2.5 GPa (right).

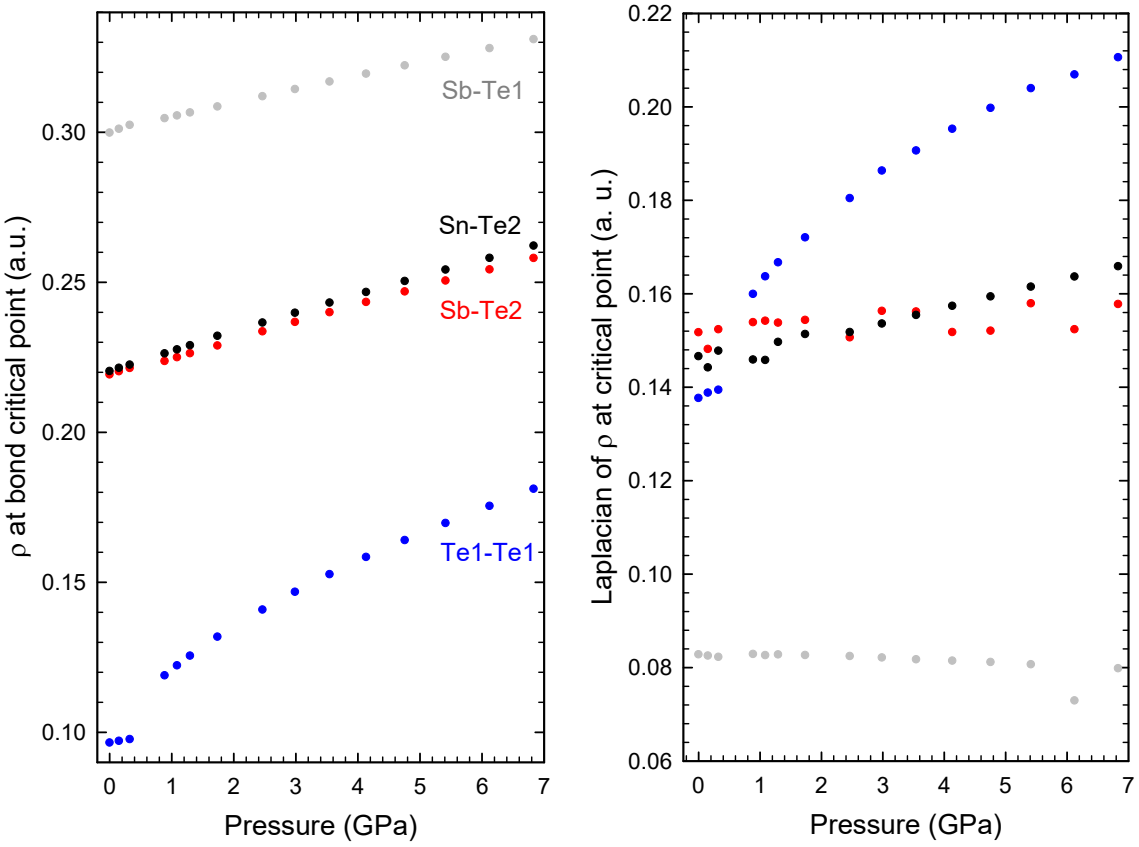

Figure S26. Pressure dependence of the electron density (left) and Laplacian of the electron density (right) at the bond critical point of the interactions of $SnSb_2Te_4$.

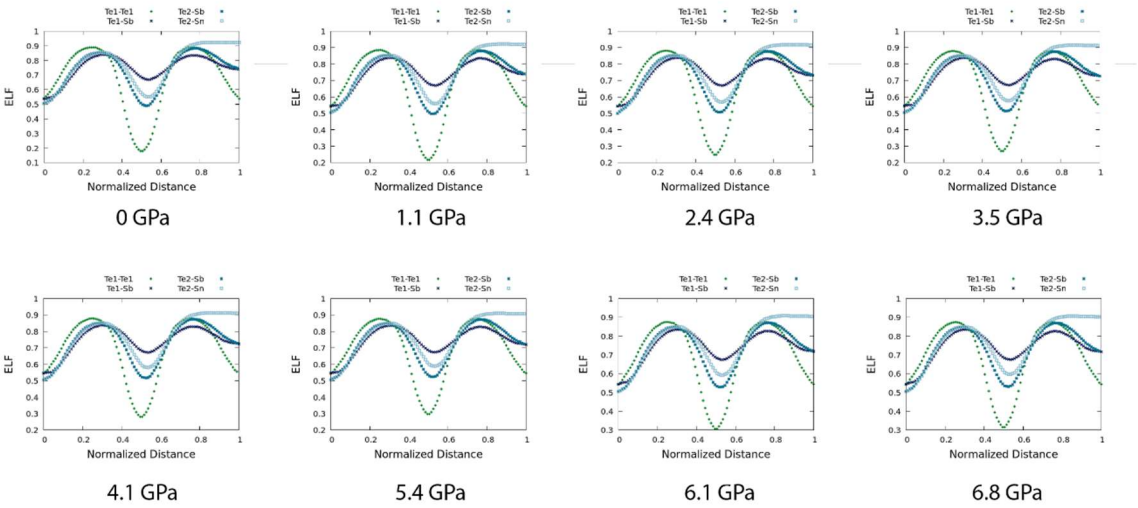

Figure S27. Pressure dependence of the ELF along the different bonds of $SnSb_2Te_4$.

Table S1. Frequencies and pressure coefficients at zero pressure of the experimental and theoretical Raman-active modes in $SnSb_2Te_4$. Theoretical values for Sb_2Te_3 are also given for comparison. Spin-orbit coupling has been included in all theoretical calculations.

	$SnSb_2Te_4$						α-Sb_2Te_3			
	Experiment			Theory			Theory			
Mode symmetry	ω_0 (cm^{-1})	a (cm^{-1} /GPa)	b (cm^{-1} /GPa^2)	ω_0 (cm^{-1})	a (cm^{-1} /GPa)	b (cm^{-1} /GPa^2)	ω_0 (cm^{-1})	a (cm^{-1} /GPa)	b (cm^{-1} /GPa^2)	Mode symmetry
E_g^1	-	-	-	38.9(2)	2.5(3)	-0.08(1)	50.4(2)	2.6(2)	-0.09(1)	E_g^1
A_{1g}^1	53.3(8)	4.2(4)	-0.15(8)	55.3(2)	4.3(4)	-0.15(2)	68.9(3)	4.3(5)	-0.07(1)	A_{1g}^1
E_g^2	103.3(4)	3.7(3)	-0.4(2)	100.5(3)	2.5(2)	-	-	-	-	
A_{1g}^2	107.8(14)	4.6(4)	-0.15(6)	115.1(2)	2.7(2)	-	-	-	-	
E_g^3	-	-	-	116.7(2)	4.6(4)	-	116.6(4)	2.1(3)	-	E_g^2
A_{1g}^3	160.9(4)	2.7(2)	-0.04(1)	167.1(3)	3.4(3)	-0.04(1)	167.6(6)	2.6(4)	-	A_{1g}^2

Table S2. Frequencies and pressure coefficients at zero pressure of the theoretical IR-active modes in $SnSb_2Te_4$, Sb_2Te_3 and SnTe. Spin-orbit coupling has been included in all theoretical calculations.

$SnSb_2Te_4$				α-Sb_2Te_3 and c-SnTe			
Mode symmetry	**ω_0 (cm^{-1})**	**a (cm^{-1}/GPa)**	**b (cm^{-1}/GPa^2)**	**ω_0 (cm^{-1})**	**a (cm^{-1}/GPa)**	**b (cm^{-1}/GPa^2)**	**Mode symmetry**
E_u^1	62.5(5)	1.6(3)	-0.037(2)	78.0	2.9	-	E_u^1
E_u^2	65.6(2)	4.3(4)	-	100.4	1.2	-	E_u^2
A_{2u}^1	81.6(3)	1.8(2)	-0.024(2)	39.9	9.1(5)	-0.31(4)	T_{1u} (TO)
A_{2u}^2	104.0(2)	5.8(5)	-	112.9(8)	1.98(17)	-	T_{1u} (LO)
E_u^3	111.9(4)	2.5(2)	-0.021(5)	109.9	1.9	-	A_{2u}^1
A_{2u}^3	155.7(5)	3.3(7)	-0.063(7)	138.7	3.5	-	A_{2u}^2

Table S3. Values of the electronic charge density and its gradient at the BCP as well as the ELF along different types of bondings.

	Ionic	**Covalent**	**Metavalent**	**Metallic**	**van der Waals**
$\boldsymbol{\rho(\vec{r})}$	Large	Large	Medium	Small	Small
$\boldsymbol{\nabla^2\rho(\vec{r})}$	Positive	Negative	Small (positive or negative)	Positive	Positive (small)
ELF	Large	Large	Medium	Small	Small

References

[S1] B. Cordero, V. Gómez, A. E. Platero-Prats, M. Revés, J. Echevarría, E. Cremades, F. Barragán, S. Alvarez. *Dalton Transactions* **2008**, *21*, 2832.

[S2] J. E. Huheey, E. A. Keiter, R. L. Keiter. Inorganic Chemistry: Principles of Structure and Reactivity, 4th edition, HarperCollins, New York, USA, 1993.

[S3] B. A. Kuropatwa, H. Kleinke. *Z. Anorg. Allg. Chem.* **2012**, 638, 2640-2647.

[S4] J.M. Skelton, L.A. Burton, A.J. Jackson, F. Oba, S.C. Parker and A. Walsh. *Phys. Chem. Chem. Phys.* **2017**, 19, 12452.

[S5] G.C. Sosso, S. Caravati and M. Bernasconi. *J. Phys.: Condens. Matter* **2009**, 21, 095410.

[S6] O. Gomis, R. Vilaplana, F. J. Manjón, P. Rodríguez-Hernández, E. Pérez-González, A. Muñoz. V. Kucek, C. Drasar. *Phys. Rev. B* **2011**, 84, 174305.

[S7] A. M. Kulibekov, H. P. Olijnyk, A. Jephcoat, Z. Y. Salaeva, S. Onari, K. R. Allakverdiev. *Phys. Stat. Sol (b)* **2003**, 235, 517-520.

[S8] D. Zhou, Q. Li, Y. Ma, Q. Cui, C. Chen. *J. Phys. Chem. C* **2013**, 117, 5352.